Localized Surface Plasmon Resonance based Bowtie Nanoantenna for Optical Biodetection

Supervisor:

Avijit Das

Submitted by:

Fateen Bin Kalam	**13121009**
Sushmita Biswas	**13321025**
Fatema Shakib	**13121166**

Submitted to the Department of Electrical and Electronics Engineering, BRAC University

In partial fulfillment of the requirements for the degree of Bachelor of Science

Summer 2017

Declaration

We hereby declare that this thesis is based on self-derived results. Materials that support our work by other researchers are mentioned in the reference section. This thesis, neither in whole or in part, has been previously submitted for any degree.

Signature of the Supervisor:

____

Avijit Das

Signature of the authors:

____

Sushmita Biswas

____

Fateen Bin Kalam

____

Fatema Shakib

ACKNOWLEDGEMENT

This paper is the work of Fatema Shakib, Fateen Bin Kalam and Sushmita Biswas, students of Electrical and Electronics Engineering (EEE) Department of BRAC University. The paper has been prepared as an effort to compile the knowledge of our years of study in the university and produce a final document which addresses the unique Localized Surface Plasmon Resonance (LSPR) properties of Gold nanostructures and its various properties and applications.

Firstly, we would like to thank our thesis supervisor Avijit Das, for his unconditional support and guidance for completion of our thesis. Secondly, our gratitude is towards BRAC University and our beloved faculty members and every other individual without whose contribution the project would not be a success. Last but not the least, a shout out to our family and friends for their constant support and encouragement.

ABSTRACT

Local Surface Plasmon Resonance is now considered one of the most promising topics due to its various applications in optics, photo catalysis, medicine and photovoltaics. Among these, Plasmonic nanoantennas have attracted considerable attention primarily due to the capability of such structures to confine and significantly enhance the incident electromagnetic field in nanometer-sized region. These metallic materials patterned at the nanoscale, exhibit interesting optical properties due to the large enhancement and localization of the electromagnetic fields. For our paper, we investigate the dependency of this energy of plasmons on the size, geometry and composition of the nanostructures as well as on the dielectric environment that surrounds them. Subsequently many such structures have been engineered to provide diverse functions including, as we report here, for biosensing. We report the behavior of two nanoparticles when they are close enough, based on their wavelength shift properties. When strong coupling takes place between them, electromagnetic fields of several times that of the incident light arise in their gap. Our paper includes, refractive index variations in the gap resulting in significantly greater displacements of resonance peaks compared to non-coupled metal nanostructures. Moreover, we report the SPR shift differences when various analytes of different refractive index is tested for biomolecular surface sensing.

Table of Contents

1. Introduction ... 11
  1.1 Definition of a Plasmon ... 11
  1.2 Nanoplasmonics ... 11
2. Physics of Localized Surface Plasmon Resonance ... 14
2.1 Surface Plasmon Resonance and Localized Surface Plasmon Resonance ... 14
  2.2 LSPR in a metal nanoparticles ... 18
  2.3 Differences between SPR and LSPR ... 26
  2.4 Electromagnetic interaction with metals ... 29
  2.5 Optical properties of metals (Drude's model) ... 31
  2.6 LSPR of Gold Nanoparticles ... 34
  2.7 Summary ... 35
3. Optical Plasmonic Nanoantennas ... 37
  3.1 What are nanoantennas? ... 37
    3.1.1 Plasmonic nanoantennas ... 38
  3.2 Biosensors ... 41
    3.2.1 Applications of biosensors ... 42
    3.2.2 Optical nanoantennas as biosensor ... 43
  3.3 Protein as bimolecular analyte ... 49
  3.4 Summary ... 56
4 Bowtie Nanoantenna ... 57
  4.1 Introduction ... 57
  4.2 Analyzed Structure ... 59
5. Finite-Difference Time-Domain (FDTD) method ... 62
  5.1 Introduction ... 62
  5.2 Lumerical Solutions: About the software ... 63
    5.2.1 Structure and Material Modeling ... 64

5.3 FDTD Solver 65
  5.3.1 General and Geometry 65
  5.3.2 Boundary Conditions 66
5.4 Mesh Analysis 70
5.5 Source – TFSF 71
  5.5.1 Transverse Electric and Transverse Magnetic Modes 71
  5.6.1 Monitors 73
  5.6.2 Analysis Group 73
5.7 Summary 74
6.0 Simulation and Results 76
6.1 Introduction 76
6.2 Results Analysis 76
  6.2.1 Varying Gap Size 77
  6.2.3 Different pitch distance 80
  6.2.4 Varying Refractive Index of the surrounding medium 82
  6.2.5 Bimolecular Surface Sensing 85
7. CONCLUSION 89
References 91

List of Figures:

Fig 1.1 TEM images of Au nanoparticles 12

Fig 1.2 Imaging of 500nm Au Np by SEM 13

Fig 2.2 Schematic of LSPR oscillation 16

Fig 2.3 Lycurgus Cup 17

Fig 2.4 Homogeneous sphere in an E field 19

Fig 2.5 Drude's absolute value vs Energy 23

Fig2.6 Bulk effect comparison 27

Fig 2.7 LSPR biosensing 29

Fig 2.8 Au Np size dependent SPR 35

Fig 3.1 Different Plasmonic Nanoantennas 37

Fig 3.2 Nano antenna fabrication 39

Fig 3.3 Working principle of biosensing 41

Fig 3.4 Major areas of biosensor applications 42

Fig 3.5 Detection of cancer cells 48

Fig 3.7 Lysozyme structure.. 51

Fig 3.8 HSA structure 52

Fig 3.9 Fibrinogen structure.. 55

Fig 4.1 Bow tie aperature top view.. 57

Fig4.2 SEM image various gap sized Au bowtie.. 58

Fig 4.3 Experimental Setup.. 60

Fig 4.4 Bowtie array 61

Fig 5.2 Lumerical Component Designs 64

Fig 5.1 Yee cell 63

Fig 5.3 Schematic of the structures... 65

Fig 5.4 Schematic of PML 67

F ig 5.5 Periodic Boundary Condition 68

Fig 5.6 Rules of Symmetry 69

Fig 5.6 Schematics of Mesh... 70

Fig 5.7(b) TE and TM modes 72

Fig 5.7(a) Structural Model.. 72

Fig 5.8(c) Scattering Cross Section 74

Fig 5.8(b) Absorption Cross Section 74

Fig 5.8(a) Cross Section Analysis.. 74

Fig 6.1 Extinction spectra for varying gaps for TM 78

Fig 6.3 Resonance peak vs corner radius... 80

Fig 6.4 Extinction spectra for array 80

Fig 6.5 Extinction for different RI 83

Fig 6.7 LSPR peak vs RI for TM.. 86

Fig 6.8 LSPR peak vs RI for TE... 87

Overview of the thesis

Chapter 1

This chapter gives an introduction to plasmons and nanoplasmonics and talks about its various applications in optics, colored glasses and so on.

Chapter 2

This chapter extensively deals with Surface Plasmon Resonance (SPR) and Localized Surface Plasmon Resonance (LSPR), the physics behind it and the differences between them. Also, it talks about optical properties of metals using Drude's model.

Chapter 3

This part explains plasmonic nanoantennas, biosensors and their applications in medical fied and agriculture. Also, it talks about various proteins as biomolecular analytes that we used in our paper namely, Lysozyme, Fibrinogen and Human Serum Albumin.

Chapter 4

This chapter talks about Bowtie antenna and its structure, and the effects of changing its features such as gap size, height, bowtie angle, and radius of curvature as well as our analyzed structures.

Chapter 5

This chapter gives an introduction to the FDTD method, Lumerical and explains the parameters and features we have used in our simulations.

Chapter 6

This part is all about the research and analysis and the simulation processes being used along with a few drawbacks. Graphs of extinction curves, peak resonance shifts on changing of conditions and factors are explained with detail explanations.

Chapter 7

Finally, this chapter is the conclusion of our thesis paper.

1. Introduction

1.1 Definition of a Plasmon

Plasmons are the quantization of classical plasma oscillations. Like ripples on a water surface are a collective mode of the water molecules of the liquid, a plasmon is a collective excitation of the electronic 'fluid' in a piece of conducting material. These electronic ripples can have discrete wavelengths. The displacement of the electrons cause the positive charge left behind to exerts an attractive force on the electrons, attempting to pull them back to their initial positions. Due to this interaction, the plasmons oscillate once they are excited, and these Coulomb interactions are also why plasmons need energy to excite. [1]

Plasmons have become so popular for quite a few reasons. They may be able to provide a way of shuttling information around on computer chips that naturally interfaces with optics. Also, plasmons are associated with large electric fields at metal surfaces, which are needed for certain sorts of spectroscopies and optical trapping. Furthermore, plasmon properties can be controlled to influence the overall optical response of a conducting system, leading to potential advancements in 'perfect lenses' [2]

1.2 Nanoplasmonics

Nanoplasmonics is a new research field combining photonics with nanotechnology, which investigates the localization of light and light/matter interactions on the nanoscale. Research in this area has advanced significantly in the last few years, thanks to advances in computation, nanofabrication, and the development of new experimental techniques to image light fields of dimensions smaller than the wavelength.[3] Nanoplasmonics is at the verge of becoming an impressive technology platform for next-generation applications in information technologies, energy, high-density data storage and life sciences. Due to the excitation of localized surface plasmons, noble-metal nanoparticles that are of size smaller than the wavelength of light in the visible region show strong resonances for light scattering and absorption. At the point of resonance, light resonantly energizes and causes combined oscillation of the conduction electrons of the metal nanoparticle, which in turn acts as a regular dipole. Its resonance frequency is strongly dependent on the shape of the particle and the dielectric environment. This phenomenon enables us to tune its color throughout the visible region and into the near-infrared (IR) regime of the electromagnetic spectrum, while keeping the size of the particle a lot below the 100 nm range. [6]

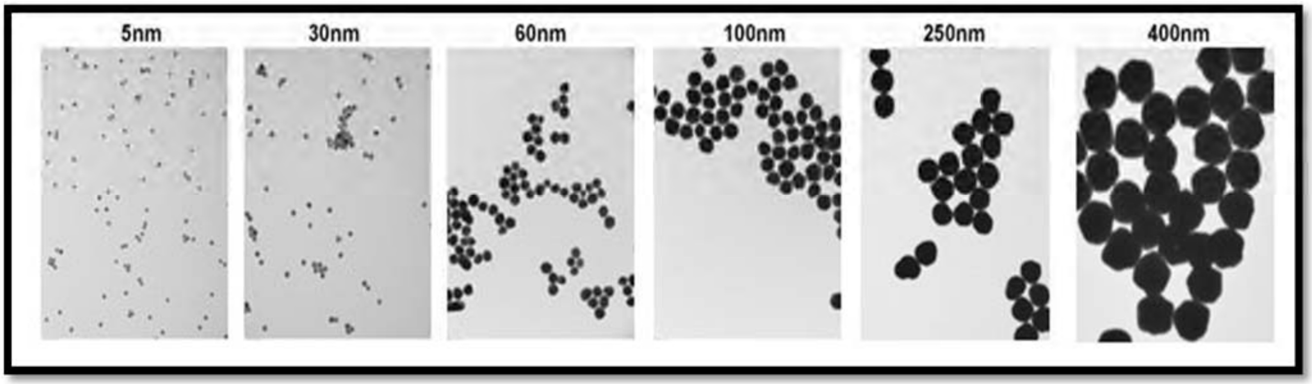

Fig 1.1 TEM images of Au nanoparticles

An interesting application of this phenomenon appears in the form of colored glass with regards to metal nanoparticle dopants. A dopant, otherwise known as a doping agent, is a trace impurity element that is inserted into a substance in very low concentrations to alter the electrical or optical properties of the substance. [4]

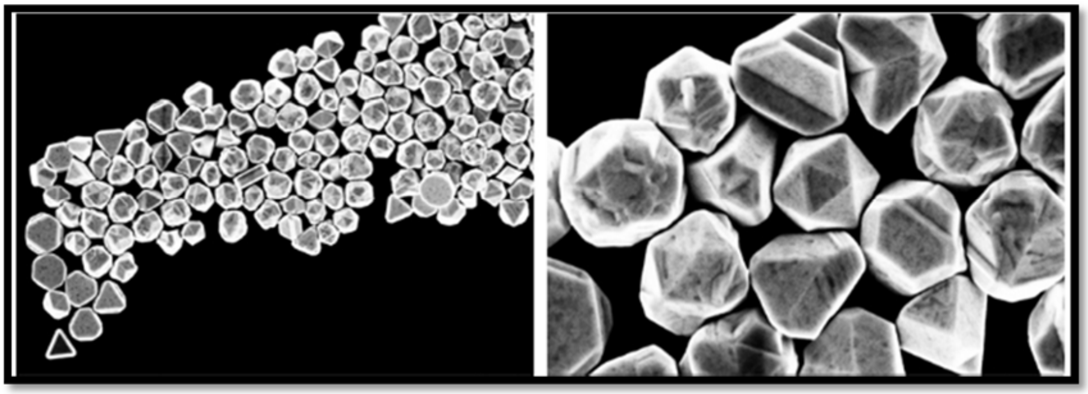

Fig 1.2 Imaging of 500nm Au Np by SEM

Some of the equipment of the **London Centre for Nanotechnology** (LCN) is fundamental for the study and fabrication of the structures needed in nanoplasmonics; high resolution **Transmission Electron Microscopy** (TEM) disentangles the properties of plasmonic modes in complex structures. **Electron Beam Lithography** or **Focused Ion Beam Milling** is necessary to produce metallic structures with properties in the visible range. In order to make sure that the samples to be investigated have the desired dimensions and morphology, high resolution **Scanning Electron Microscope** (SEM) imaging is required. [5]

2. Physics of Localized Surface Plasmon Resonance

2.1 Surface Plasmon Resonance and Localized Surface Plasmon Resonance

Surface Plasmon Resonance has emerged as a powerful optical detection technique for studying label free bimolecular interactions in real time within a variety of diverse applications such as life science, electrochemistry, chemical vapor detection, food and environmental safety and beyond. [8] Due to its simplicity, every commercially available SPR instrument uses a detection scheme called the Kretschmann configuration. In this setup, a light source passes through a prism and reflects off the backside of a sensor chip surface into a detector as shown below.

At a certain incident angle known as the resonance angle, light is absorbed by the electrons in the metal film of the sensor chip causing them to resonate. These resonating electrons are also known as surface plasmons which are sensitive to their surrounding environment. The result is an intensity loss in the reflected beam which appears as a dark band and can be seen as a dip in the SPR reflection intensity curve.

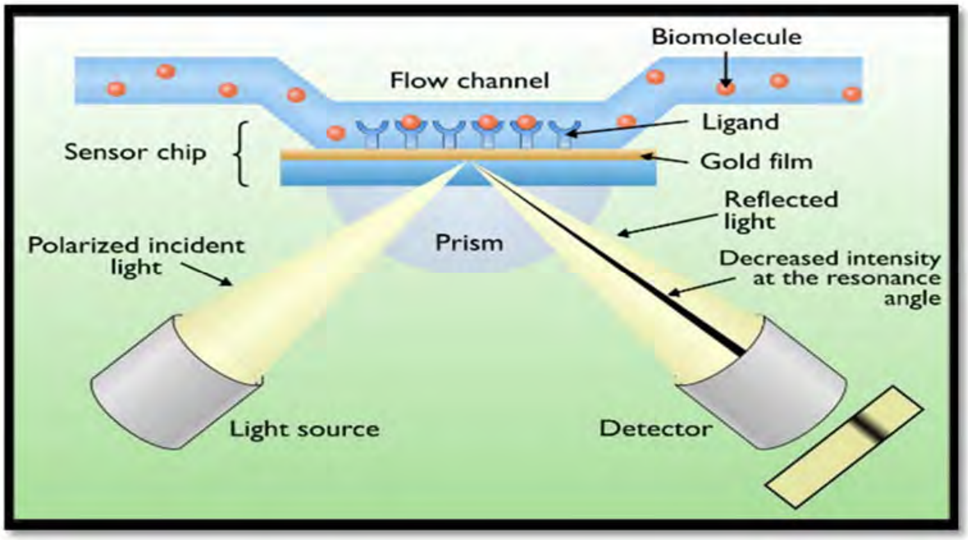

Fig 2.1 Method of SPR

The shape and location of the SPR dip can then be used to convey information about the sensor surface. SPR technology is commonly utilized for the study of molecular binding interactions between free analyte molecules in solution and probe molecules which are linked to or immobilized onto the sensor surface. As the molecular binding event takes place, a shift in the reflectivity curve can be observed. This is a direct method of detection which avoids the drawback of labels. Another powerful aspect of SPR technology is in its ability to absorb the time dependent binding interactions between molecules. By monitoring this change in SPR response over time, researchers can study the kinetics of molecular binding events. [10]

Localized surface plasmon resonance (LSPR) is an optical phenomena created by light when it collaborates with conductive nanoparticles (NPs) that are smaller than the incident wavelength. As in surface plasmon resonance, the electric field of incident light can be deposited to collectively excite electrons of a conduction band, with the outcome being coherent localized plasmon oscillations with a resonant frequency that relies on the arrangement, size, geometry, and separation distance of NPs. [11]

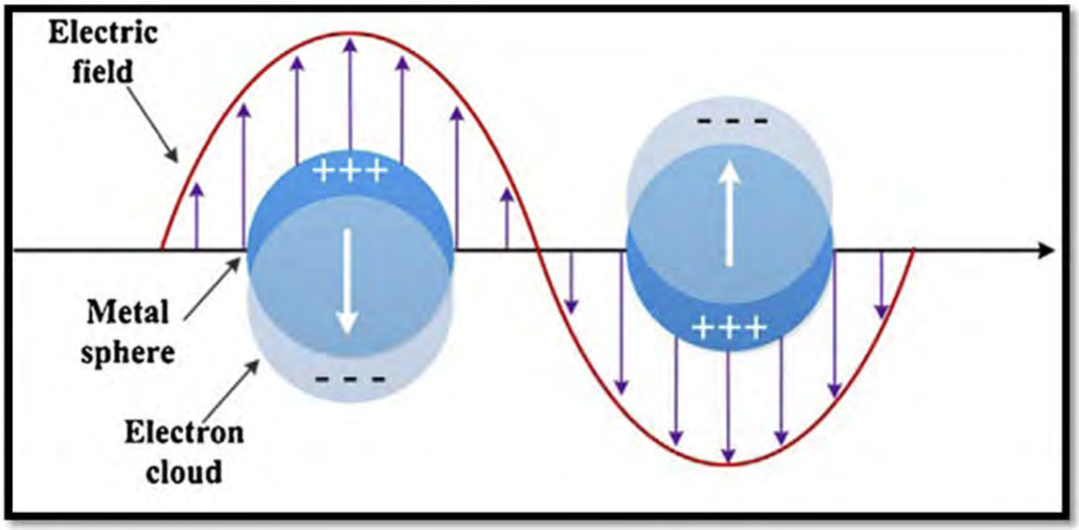

Fig 2.2 Schematic of LSPR oscillation

LSP has two important effects. Firstly, electric fields near the particle's surface are greatly enhanced. This enhancement falls off quickly if the distance from the surface is increased. Secondly, the particle's optical absorption has a maximum at the plasmon resonant frequency. For noble metal nanoparticles, this occurs at visible wavelengths. For semiconductor nanoparticles, the maximum optical absorption occurs in the near-infrared or mid infrared region. [9] Localized Surface Plasmons are non-propagating excitations of the conduction electrons of metallic nanostructures coupled to the electromagnetic field. These modes generate naturally from the scattering problem of a small, sub-wavelength conductive nanoparticle in an oscillating electromagnetic field. An operative restoring force is exerted on the driven electrons by the curved surface of the nanoparticle. As a result, a resonance arises, leading to field amplification on both inside and in the near-field zone outside the particle. This resonance is called localized surface plasmon resonance. Another significance of the curved surface is that the plasmon resonances can be generated by direct light illumination.

The resonance in gold and silver nanoparticles lies in the visible range of the electromagnetic spectrum owing to which bright colors are displayed by the particles. As a result, it can be applied in staining of glass in windows or ornamental cups.

Fig 2.3 Lycurgus Cup

This cup is green under normal lighting conditions and turns red when illuminated from within. Tiny metal particles are responsible for the colors. From regular experience it is clear that metals interact strongly with light. The light is compelled to turn around and travel in the opposite direction whenever it comes across a mirrored surface. This is due to the fact that metals have free electrons floating around in them. Light and electrons have a close association due to their electric fields, for a mirror the oscillation of the light field causes the electrons in the metal to also oscillate. Because the electron have some mass it takes time to get them moving and so, in this case, they tend to oscillate in anti-phase with the optical field (the field and electrons moving in opposite directions).[12]

This movement prevents the light from entering the material. The electrons make a screening field that the light cannot go through. Thus the light is reflected. In the case of the cup the pieces of metal are so small that this picture no longer works. It must be recalled that everything is quantum in nature at the small scale, and therefore everything is a wave. The free electrons moving around the particles can only oscillate at certain frequencies corresponding to the allowed standing waves (like waves on a sting). At these frequencies the light is highly absorbed and scattered, leading to a much-reduced transmission but enhanced reflection, giving the cup its properties. By changing the size of the metal particle the scattered colors (and therefore transmitted colors) are altered. The same rules apply for surfaces, but structuring can cause standing waves in the free electrons of a metal, and this can create surface plasmons. Since transmission is impossible in this situation (there is a piece of metal under the surface), the plasmons will display as simply absorption of a specific shade of the reflected light. [7]

2.2 LSPR in a metal nanoparticles

The **Quasi-Static** approximation can be used to analyze the interaction of a particle of size d with the electromagnetic field, given that $d<<\lambda$, that is, the particle is way smaller compared to the wavelength of the incident light surrounding the medium. In such a case, the phase of the harmonically oscillating electromagnetic field is virtually constant over the particle volume. Therefore, it is possible to calculate the spatial field distribution by assuming the simplified problem of a particle in an electrostatic field. Once the field distributions are considered, the harmonic time dependence can then be added to the solution. This lowest-order estimation of the full scattering problem describes the optical properties of nanoparticles of proportions below 100 nm, effectively for many purposes.

Initially we begin with a homogeneous, isotropic sphere of radius a, positioned at the origin in a uniform, static electric field, $\mathbf{E} = E0\ \hat{}\mathbf{z}$. the surrounding medium is isotropic and non-absorbing with dielectric constant εm, and the field lines are parallel to the z-direction at an adequate amount of distance from the sphere. The dielectric response of the sphere is further described by the dielectric function $\varepsilon\ (\omega)$, which we consider as a simple complex number ε for the time being. [9]

Keeping an electrostatic perspective, we are looking towards a solution of the **Laplace equation** for the potential, ∇2Φ = 0, from which we will be able to calculate the electric field, **E** = −∇Φ. Because of the azimuthal symmetry of the problem, the general solution is of the form:

$$\Phi(r,\theta) = \sum_{l=0}^{\infty}\left[A_l r^l + B_l r^{-(l+1)}\right] P_l(\cos\theta),$$

:

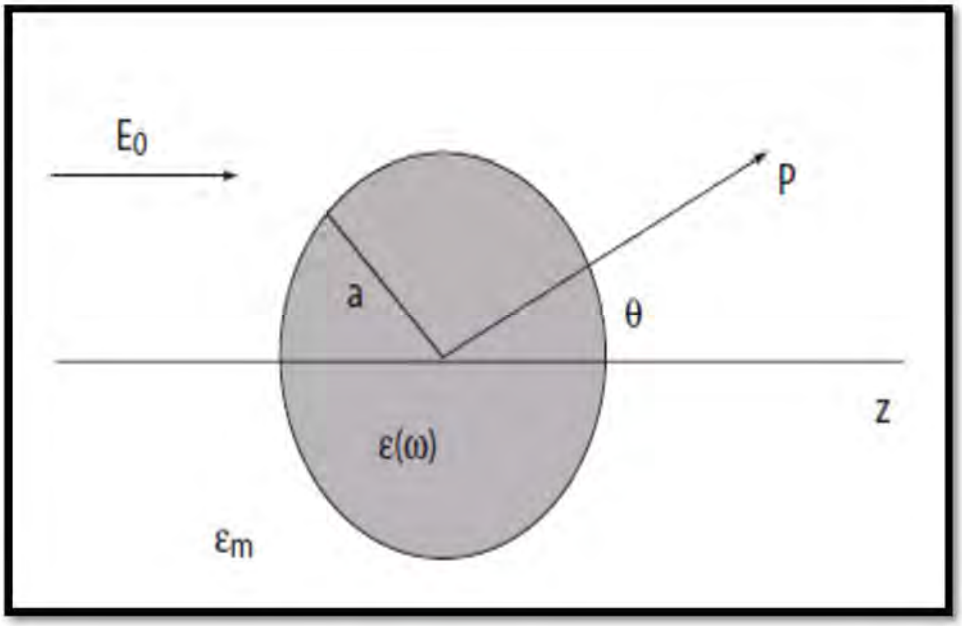

Fig 2.4 Homogeneous sphere in an E field [3]

Where *Pl (*cos*θ)* are the Legendre Polynomials of order *l*, and *θ* the angle between the position vector **r,** at point P and the z-axis. While maintaining the fact that the potentials remain finite at the origin, the solution for the potentials Φin inside and Φout outside the sphere can be written as:

$$\Phi_{\text{in}}(r,\theta)=\sum_{l=0}^{\infty}A_l r^l P_l(\cos\theta)$$

$$\Phi_{\text{out}}(r,\theta)=\sum_{l=0}^{\infty}\left[B_l r^l + C_l r^{-(l+1)}\right]P_l(\cos\theta).$$

The coefficients *Al*, *Bl*and *Cl*can now be determined form the boundary conditions at *r* → ∞ and at the sphere surface *r* = *a*. The requirement that Φin→−*E0z*= −*E*0*r* cos*θ*as *r* → ∞ demands that *Bl*= −*E*0 and *Bl*= 0 for *l ≠1*. The remaining coefficients *Al* and *Cl*are defined by the boundary conditions at *r* = *a*. equality of the tangential components of the electric field demands that

$$-\frac{1}{a}\frac{\partial\Phi_{\text{in}}}{\partial\theta}\bigg|_{r=a}=-\frac{1}{a}\frac{\partial\Phi_{\text{out}}}{\partial\theta}\bigg|_{r=a},$$

And the equality of the normal components of the displacement field

$$-\varepsilon_0\varepsilon\frac{\partial\Phi_{\text{in}}}{\partial r}\bigg|_{r=a}=-\varepsilon_0\varepsilon_{\text{m}}\frac{\partial\Phi_{\text{out}}}{\partial r}\bigg|_{r=a}.$$

Applying these boundary conditions leads to *Al* = *Cl*= 0 for *l ≠1*, and by calculating the remaining coefficients *Al* and *Cl*, the potentials evaluate to:

$$\Phi_{\text{in}} = -\frac{3\varepsilon_m}{\varepsilon + 2\varepsilon_m} E_0 r \cos\theta$$

$$\Phi_{\text{out}} = -E_0 r \cos\theta + \frac{\varepsilon - \varepsilon_m}{\varepsilon + 2\varepsilon_m} E_0 a^3 \frac{\cos\theta}{r^2}.$$

It is interesting to interpret the w=equation physically: Φout describes the superposition for the applied field and that of a dipole located at the particle center. We can rewrite Φout by introducing the dipole moment **p** as:

$$\Phi_{\text{out}} = -E_0 r \cos\theta + \frac{\mathbf{p} \cdot \mathbf{r}}{4\pi \varepsilon_0 \varepsilon_m r^3}$$

$$\mathbf{p} = 4\pi \varepsilon_0 \varepsilon_m a^3 \frac{\varepsilon - \varepsilon_m}{\varepsilon + 2\varepsilon_m} \mathbf{E}_0.$$

Hence, we see that a dipole moment is introduced by the applied field inside the sphere of magnitude proportional to |**E**0|. If we introduce the polarizability:

$$\alpha = 4\pi a^3 \frac{\varepsilon - \varepsilon_m}{\varepsilon + 2\varepsilon_m}.$$

This equation is the prime result of this section, the complex polarizability of a small sphere of sub-wavelength diameter in the electrostatic approximation. We observe that it shows the same functional form as the Clausius-Mossotti relation. [9]

The following figure (Fig. 2.7) shows the absolute value and phase of *a* with respect to frequency *ω* (in energy units) for a dielectric constant varying as *ε(ω)* of the Drude form, in this case fitted to the dielectric response of silver [Johnson and Christy, 1972]. It is obvious that the polarizability experiences a resonant enhancement under the condition that $|\varepsilon + 2\varepsilon m|$ is a minimum, which for the case of small or slowly varying Im[ε] around the resonance simplifies to:

$$\mathrm{Re}\left[\varepsilon\left(\omega\right)\right] = -2\varepsilon_m.$$

This relationship is called the Fröhlich condition and the associated mode (in an oscillating field) the *dipole surface plasmon* of the metal nanoparticle. For a sphere consisting of a Drude metal with a dielectric function located in air, the Fröhlich criterion is met at the frequency *ω0=ωp/√3*, which further shows the strong dependence of the resonance frequency on the dielectric environment: The resonance red shifts as *εm*is increased. Metal nanoparticles are thus the ideal platforms for optical sensing of change in refractive index.

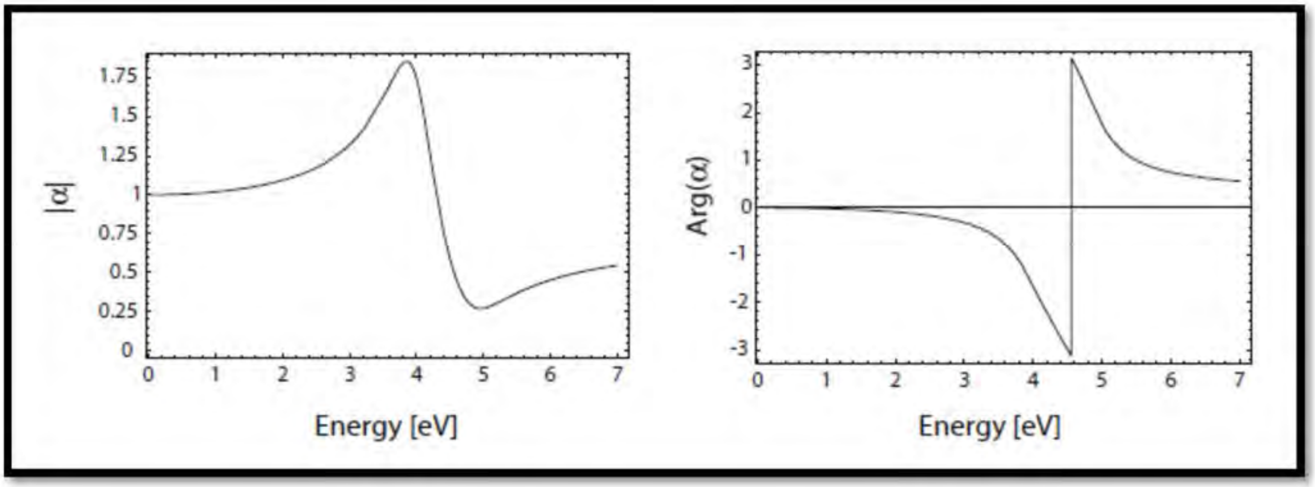

Fig 2.5 Drude's absolute value vs. Energy

In Fig 2.5, absolute value and field polarizability α of a sub-wavelength metal nanoparticle with respect to frequency of the driving field (expressed as eV units) is shown. Here, ε (ω) is taken as a Drude fit to the dielectric function of silver [Johnson and Christy. 1972) [9]

We note that the magnitude of α at resonance is limited by the incomplete vanishing of its denominator, due to Im [$\varepsilon(\omega)$] ≠ 0.

The distributions of the electric field $\mathbf{E} = -\nabla\Phi$ can be evaluated from the potentials to:

$$\mathbf{E}_{\mathbf{in}} = \frac{3\varepsilon_m}{\varepsilon + 2\varepsilon_m}\mathbf{E}_0$$

$$\mathbf{E}_{\mathbf{out}} = \mathbf{E}_0 + \frac{3\mathbf{n}\,(\mathbf{n}\cdot\mathbf{p}) - \mathbf{p}}{4\pi\,\varepsilon_0\varepsilon_m}\frac{1}{r^3}.$$

A resonant enhancement of both the internal and dipolar fields is implied by the resonance in α. Many of the remarkable applications of metal nanoparticles in optical devices and sensors depend on this field enhancement at the plasmon resonance.

Now we will keep electrostatics aside for a while and turn our attention to the electromagnetic fields radiated by a small particle excited at its plasmon resonance. For a small sphere $a << \lambda$, its representation as an ideal dipole is valid in the Quasi-Static regime, i.e. it allows for time-varying fields but ignores spatial retardation effects over the particle volume. Under plane-wave illumination with $\mathbf{E}(\mathbf{r}, t) = \mathbf{E}0e{-}i\omega t$, the fields introduce an oscillating dipole moment $\mathbf{p}\ (t) = \varepsilon 0\varepsilon m\alpha\mathbf{E}0e{-}i\omega t$, with α given by the electrostatic result. The radiation of this dipole leads to *scattering* of the plane wave by the sphere, which can be represented as radiation by a point dipole.

It is useful to briefly review the basics of the electromagnetic fields associated with an oscillating electric dipole. The total fields $\mathbf{H}\ (t) = \mathbf{H}e{-}i\omega t$and $\mathbf{E}\ (t) = \mathbf{E}e{-}i\omega t$in the near immediate zones of a dipole can be written as: [14]

$$\mathbf{H} = \frac{ck^2}{4\pi}\left(\mathbf{n} \times \mathbf{p}\right)\frac{e^{ikr}}{r}\left(1 - \frac{1}{ikr}\right)$$

$$\mathbf{E} = \frac{1}{4\pi\varepsilon_0\varepsilon_m}\left\{k^2\left(\mathbf{n} \times \mathbf{p}\right) \times \mathbf{n}\frac{e^{ikr}}{r} + \left[3\mathbf{n}\left(\mathbf{n} \cdot \mathbf{p}\right) - \mathbf{p}\right]\left(\frac{1}{r^3} - \frac{ik}{r^2}\right)e^{ikr}\right\},$$

With $k = 2\pi/\lambda$ and $\mathbf{n}$ the unit vector in the direction of the point P of interest. In the near zone $(kr << 1)$, the electrostatic result for the electric field is recovered,

$$\mathbf{E} = \frac{3\mathbf{n}\left(\mathbf{n} \cdot \mathbf{p}\right) - \mathbf{p}}{4\pi\varepsilon_0\varepsilon_m}\frac{1}{r^3}$$

And the accompanying magnetic field present for oscillating fields amounts to:

$$\mathbf{H} = \frac{i\omega}{4\pi} (\mathbf{n} \times \mathbf{p}) \frac{1}{r^2}.$$

We can observe that within the near field, the fields are predominantly electric in nature, since the magnitude of the magnetic field is about a factor √ (*ε*0/*µ*0) *(kr)* smaller than that of the electric field. For static fields *(kr*→ 0*)*, the magnetic field vanishes.
In the opposite limit of the radiation zone, defined by *kr*>> 1, the dipole fields are of the well-known spherical-wave form:

$$\mathbf{H} = \frac{ck^2}{4\pi} (\mathbf{n} \times \mathbf{p}) \frac{e^{ikr}}{r}$$
$$\mathbf{E} = \sqrt{\frac{\mu_0}{\varepsilon_0 \varepsilon_m}} \mathbf{H} \times \mathbf{n}.$$

It is more fascinating from an optical perspective to note that another consequence of the resonantly enhanced polarization *α* is an associated improvement in the efficiency with which a metal nanoparticle scatters and absorbs light. The corresponding cross sections for scattering and absorption *Csca* and *C*abs can be calculated via the Poynting-vector determined from above [Bohren and Huffman, 1983] to:

$$C_{\text{sca}} = \frac{k^4}{6\pi} |\alpha|^2 = \frac{8\pi}{3} k^4 a^6 \left| \frac{\varepsilon - \varepsilon_m}{\varepsilon + 2\varepsilon_m} \right|^2$$
$$C_{\text{abs}} = k\text{Im}[\alpha] = 4\pi k a^3 \text{Im} \left[\frac{\varepsilon - \varepsilon_m}{\varepsilon + 2\varepsilon_m} \right].$$

The scattering efficiency, which scales with $a6$, *is* dominated over by the efficiency of absorption scaling with $a3$, for small particles within the condition $a << \lambda$. No explicit assumptions were made in our derivations so far that the sphere is indeed metallic. The expressions for the cross sections are therefore valid for the dielectric scatterers too, and demonstrate a very important problem for practical purposes. Due to rapid scaling of $C\text{sca} \propto a6$, it is quite difficult to pick out small objects from a background of larger scatterers.

Imaging of nanoparticles with dimensions below 40 nm, immersed in a background of light scatterers can thus only be achieved using photo-thermal techniques relying on the slower scaling of the absorption cross section with size. [13] Equations also show that indeed for metal nanoparticles, both absorption and scattering (and thus extinction) are resonantly enhanced at the dipole particle plasmon resonance, i.e. when Frölich condition is met. For a sphere of volume V and dielectric function $\varepsilon = \varepsilon 1 + i\varepsilon 2$ in the Quais-Statc limit, the explicit expression for the extinction cross section $C\text{ext} = C\text{abs} + C\text{sca}$ is:

$$C_{\text{ext}} = 9\frac{\omega}{c}\varepsilon_m^{3/2} V \frac{\varepsilon_2}{[\varepsilon_1 + 2\varepsilon_m]^2 + \varepsilon_2^2}.$$

2.3 Differences between SPR and LSPR

Localized surface plasmon resonance is generated by metal nanoparticles, typically gold and silver, as compared to a continuous film of gold as used in traditional SPR. LSPR produces a strong resonance absorbance peak in the visible range of light, with its position being highly sensitive to the local refractive index surrounding the particle. Therefore, SPR measures small changes in the wavelength of the absorbance position, rather than the angle as in traditional SPR.

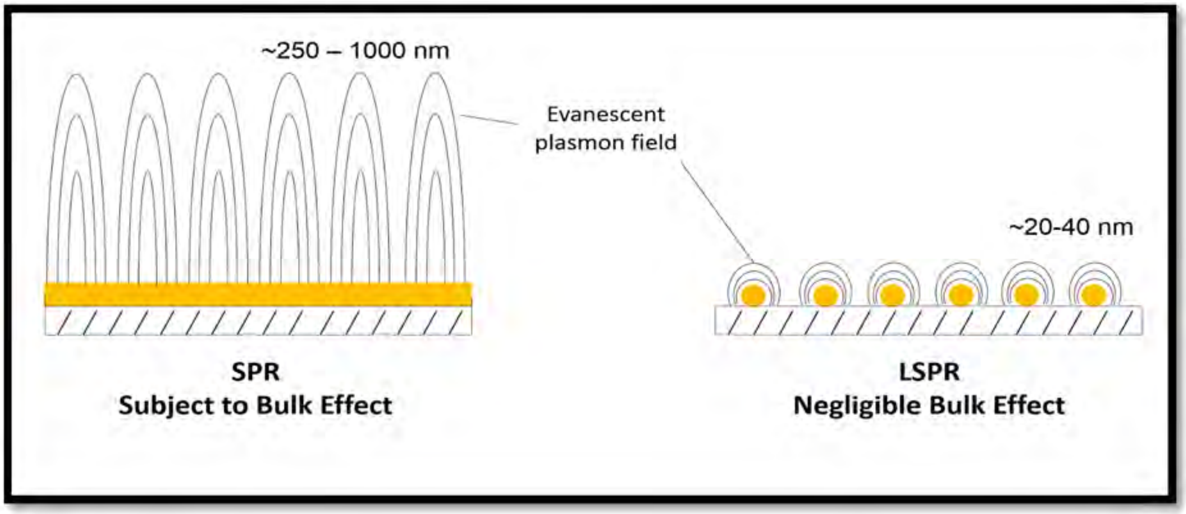

Fig2.6 Bulk effect comparison [4]

A key difference between SPR and LSPR becomes particularly notable in biosensing applications. The difference is in the sensing volume of the respective plasmons captured by what is referred to as bulk effect. Due to the much larger plasmon field of SPR up to a thousand nanometers versus LSPR's 40 nanometers, biomolecules that are not actually bound on the sensor surface can be detected in SPR causing a bulk effect. In contrast, in LSPR, only the molecules bound at the surface are captured by the localized surface plasmons. Thus LSPR has marginal bulk effect. [15]

Using LSPR instead of SPR has a number of significant advantages:

- The optical hardware needed for LSPR is much less complex since no prism is needed to couple the light, so the instrument can be made smaller and more affordable
- Since the angle is not important, the instrument is much more robust against vibration and mechanical noise
- LSPR is not as sensitive to bulk refractive index changes, which causes errors in experimental data, because it has a much shorter electromagnetic field decay length

- No strict temperature control is needed, simplifying the instrument
- The sensor chips can be manufactured at a much more affordable price
- Easier to use and maintain

Although SPR sensors have a much higher refractive index sensitivity (m or RIS) than LSPR sensors, their sensitivity towards biomolecular binding events is similar. This is due to the much shorter electromagnetic decay length (ld.) of nanoparticles compared to gold films, which confines the response to a smaller sensing volume. [17] An LSPR's sensor response (R) to an absorbed layer can be modeled with the following equation:

$$R = m\Delta n(1 - e^{\frac{-2d}{l_d}})$$

Where Δn is the difference in refractive index between the absorbed layer and the surrounding medium, and d is the thickness of the absorbed layer.

The smaller decay length of SPR versus LSPR is illustrated in the image below. This smaller sensing volume means that LSPR is more sensitive to molecular binding and less sensitive to bulk effects.[16] The smaller decay length and sensitivity associated with LSPR reduces artifacts caused by external variables such as temperature drift or buffer refractive index changes.

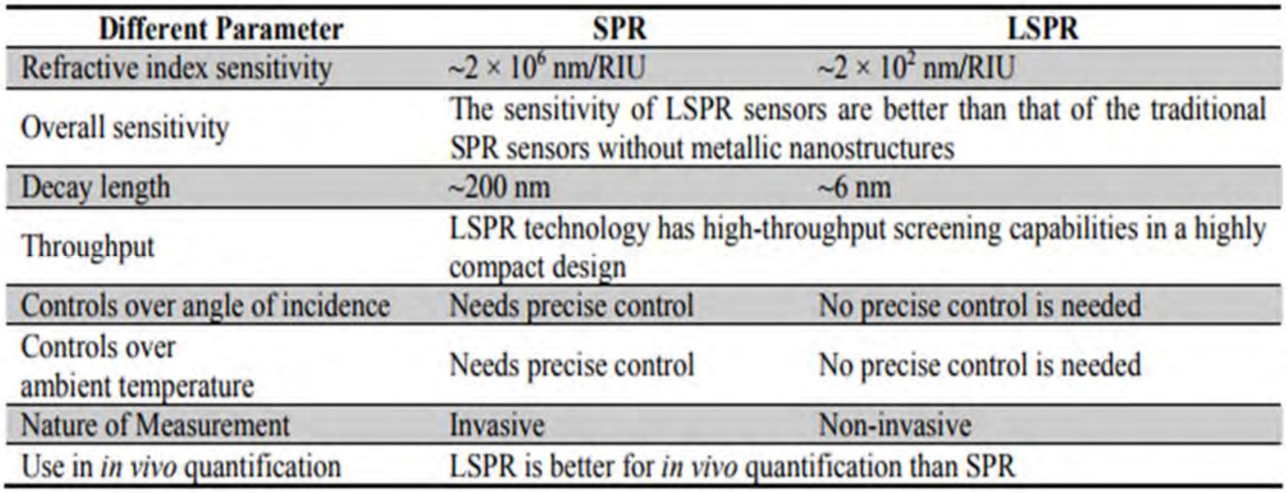

Different Parameter	SPR	LSPR
Refractive index sensitivity	~2 × 10^6 nm/RIU	~2 × 10^2 nm/RIU
Overall sensitivity	The sensitivity of LSPR sensors are better than that of the traditional SPR sensors without metallic nanostructures	
Decay length	~200 nm	~6 nm
Throughput	LSPR technology has high-throughput screening capabilities in a highly compact design	
Controls over angle of incidence	Needs precise control	No precise control is needed
Controls over ambient temperature	Needs precise control	No precise control is needed
Nature of Measurement	Invasive	Non-invasive
Use in *in vivo* quantification	LSPR is better for *in vivo* quantification than SPR	

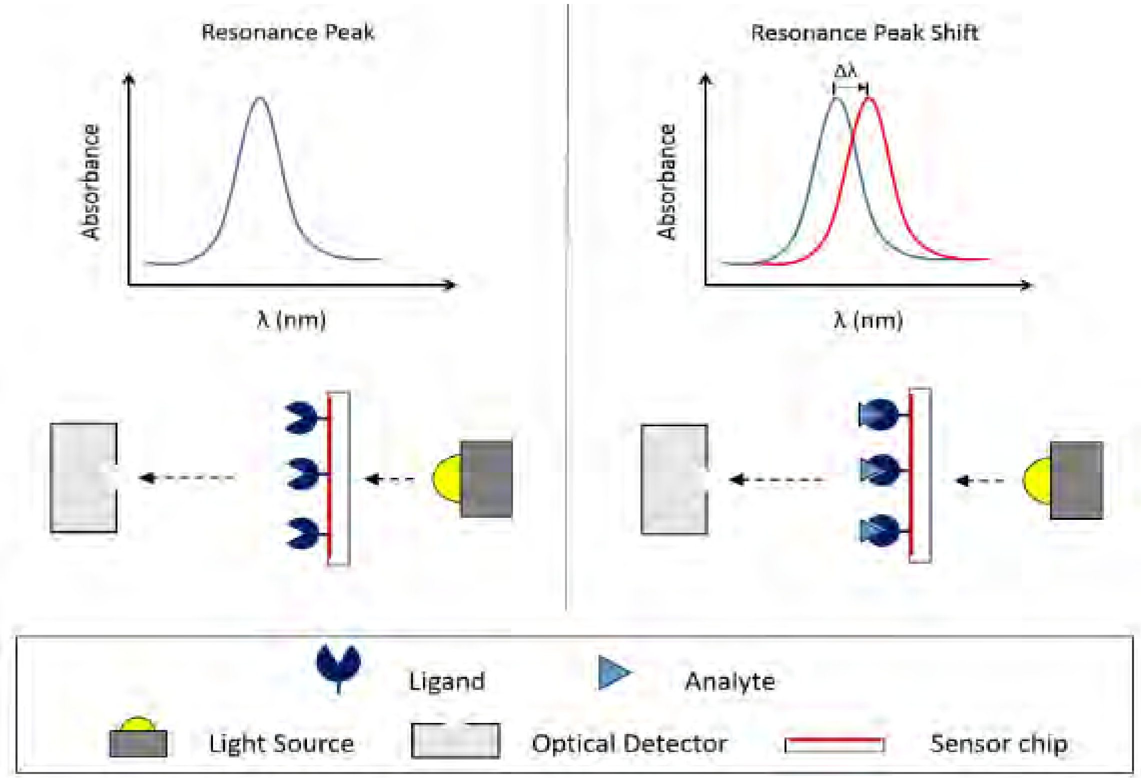

Fig 2.7 LSPR biosensing

2.4 Electromagnetic interaction with metals

The association of metals with electromagnetic fields can be properly comprehended in a traditional structure in view of Maxwell's conditions. Indeed, even metallic nanostructures which measure up to a couple of nanometers can be described without a need to depend on quantum mechanics, since the high density of free carriers brings about tiny spacing of the electron energy levels contrasted with thermal excitations of energy at room temperature. The optics of metals described here subsequently falls under the domains of the classical theory. Still, there is a rich and unexpected variety of optical phenomena due to the strong dependence of the optical properties on frequency. [5]

Metals are highly reflective for frequencies up to the visible part of the spectrum and do not allow electromagnetic waves to propagate through them. They are therefore usually used as cladding layers for the construction of waveguides and resonators for electromagnetic radiation at microwave and far-infrared frequencies. The perfect conductor approximation of infinite or fixed finite conductivity makes sense for most purposes in this low-frequency region because only a tiny fraction of the electromagnetic waves penetrates into the metal. The penetration of the field increases sufficiently at higher frequencies towards the near infrared and visible part of the spectrum, resulting in increased dissipation, and restricting a size scaling of photonic devices that work sufficiently well at low frequencies to this region. Lastly, metals gain dielectric character at ultraviolet frequencies and allow the propagation of electromagnetic waves, though with varying degrees of reduction, depending on the details of the electronic band structure. Alkali metals such as sodium have an almost free-electron-like response and thus display an ultraviolet transparency. However, noble metals like gold or silver have transitions between electronic bands leading to healthy absorption in this region.

A complex dielectric function $\varepsilon(\omega)$ can be used to describe these scattering properties. The main reason behind this dependence on frequency of the optical response is a change in the phase of the induced currents with respect to the field for frequencies coming near to the reciprocal of the characteristic electron relaxation time of the metal. [5]

Maxwell’s equations are regarded as the mathematical summary of the classical theory of electromagnetism. They describe how both electric and magnetic fields arise from electrical charge and currents, how they propagate and how they influence each other. The four equations are presented below:

- Gauss' law for electricity: $\nabla \cdot E = \frac{\rho}{\varepsilon_0} = 4\pi k \rho$
- Gauss' law for magnetism: $\nabla \cdot B = 0$

- Faraday's law of induction: $\nabla x\, E = -\frac{\partial B}{\partial t}$

- Ampere's law:

$$\nabla\ x\ B = \frac{4\pi k}{c^2} J + \frac{1}{c^2}\frac{\partial E}{\partial t}$$
$$= \frac{J}{\varepsilon_0 c^2} + \frac{1}{c^2}\frac{\partial E}{\partial t}$$

[6]

2.5 Optical properties of metals (Drude's model)

In solid-state physics, the Drude's model is a simple model for the behavior of valence electrons in a crystal structure of a metallic solid. It was first developed by Arnold Somerfield, who combined the classical Drude Model with quantum mechanical Fermi-Dirac statistics.
The free electron empty lattice approximation forms the basis of the band structure model known as nearly free electron model. Given its simplicity, it is surprisingly successful in explaining many experimental phenomena, especially:

- the Wiedemann–Franz law which relates electrical conductivity and thermal conductivity;
- the temperature dependence of the heat capacity;
- the shape of the electronic density of states;
- the range of binding energy values;

- electrical conductivities;
- thermal electron emission and field electron emission from bulk metals.

Similar to the Drude Model, valence electrons are assumed to be entirely separated from their ion, forming an electron gas. Similar to the properties of an ideal gas, electron-electron interactions are completely ignored. The electrostatic fields are weak in metals because of the screening effect.

The crystal lattice is not clearly taken under consideration. A quantum-mechanical explanation is given by Bloch's Theorem: an unbound electron moves in a periodic potential as a free electron in vacuum, except for the electron mass *m* becoming an effective mass *m** which may deviate considerably from *m* It is even possible to use negative effective mass to describe conduction by electron holes. Effective masses can be derived from band structure computations. Even though the static lattice does not hamper the motion of the electrons, the electrons can be scattered by phonons and by impurities. These two determine the electrical and thermal conductivity (superconductivity requires a more refined theory than the free electron model).
According to the Pauli Exclusion Principle, each phase space element (Δk) 3(Δx) 3 can be occupied only by two electrons (one per spin quantum number). This restriction of available electron states is taken into account by Fermi–Dirac statistics (see also Fermi gas). Main predictions of the free-electron model are derived by the Somerfield expansion of the Fermi–Dirac occupancy for energies around the Fermi level. [19]

Energy and Wave Function of a Free Electron

For a free particle the potential is V(R) = 0. The Schrödinger equation for such a particle, like the free electron [18] is:

$$-\frac{\hbar^2}{2m}\nabla^2\Psi(\mathbf{r},t) = i\hbar\frac{\partial}{\partial t}\Psi(\mathbf{r},t)$$

The wave function ψ(r, t) can be split into a solution of a time dependent and a solution of a time independent equation. The solution of the time dependent equation is:

$$\Psi(\mathbf{r}, t) = \psi(\mathbf{r}) e^{-i\omega t}$$

With energy,

$$E = \hbar\omega$$

The solution of the time independent equation is:

$$\psi_{\mathbf{k}}(\mathbf{r}) = \frac{1}{\sqrt{\Omega_r}} e^{i\mathbf{k}\cdot\mathbf{r}}$$

With a wave vector k.Ωr is the volume of space where the electron can be found. The electron has a kinetic energy:

$$E = \frac{\hbar^2 k^2}{2m}$$

The plane wave solution of this Schrödinger equation is:

$$\Psi(\mathbf{r}, t) = \frac{1}{\sqrt{\Omega_r}} e^{i\mathbf{k}\cdot\mathbf{r} - i\omega t}$$

For solid state and condensed matter physics, the time independent solution ψk (r) is extremely intriguing. It is the basis of electronic band structure models that are widely used in solid-state physics for model Hamiltonians like the nearly free electron model and the tight binding model and different models that use a Muffin-tin approximation. The Eigen functions of these Hamiltonians are Bloch waves which are modulated plane waves. [18] [20]

2.6 LSPR of Gold Nanoparticles

Gold nanoparticles have been broadly used for applications in the fields of both biology (e.g. bio-imaging) and technology (e.g. photonics) due their unique optical properties. These properties are granted by the interaction of light with electrons on the gold nanoparticle surface.

At a particular wavelength (frequency) of light, collective oscillation of electrons on the gold nanoparticle surface cause surface plasmon resonance, resulting in both absorption and scattering of light. The particular wavelength or frequency of light where this occurs is strongly dependent on the gold nanoparticle size, shape and surface. [21]

The dependence of gold nanoparticle size on the surface plasmon resonance is illustrated in the figure below where the absorption maximum (lambda max) increases from 520nm to 570nm for Cyto diagnostics 20nm and 100nm spherical gold nanoparticles, respectively. Particles with sizes above 100nm have broader peaks spanning into the 600nm range due to the presence of both transversal and longitudinal surface plasmon resonances. In comparison, gold nanoparticles with diameters below 2nm do not exhibit surface plasmon resonance. [22]

The difference in extinction between different sized gold nanoparticles can conveniently be utilized for multiplexing.

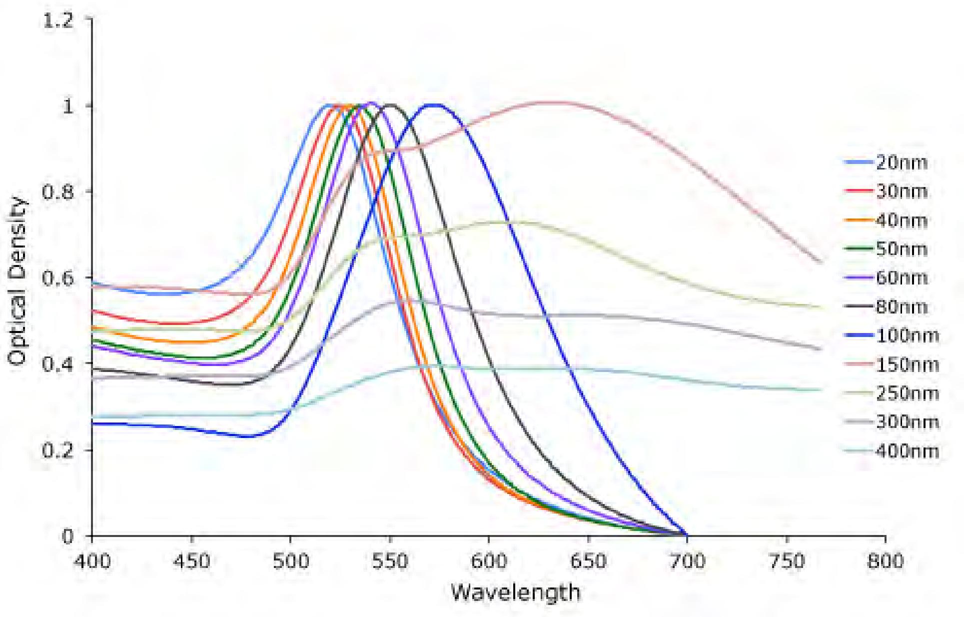

Fig 2.8 Au Np size dependent SPR

2.7 Summary

Surface plasmon resonance is the resonant oscillation of conduction electrons at the interface between negative (εm< 0) and positive (εd> 0) permittivity material stimulated by incident light. Upon incidence of light whose frequency matches with that of the natural frequency of the conduction electrons, the oscillation of the conduction electrons in the metal and dielectric interface generates a propagating evanescent wave. The electric field propagates both inside and outside the metal. The generation of evanescent waves proves that the energy is confined in a small area where the light has hit the metal surface.

A Localized Surface Plasmon Resonance (LSPR) is the result of the confinement of a surface plasmon in a nanoparticle of size comparable or smaller than the wavelength of the light in the visible range or the light used to excite the plasmon. Unlike Surface Plasmons, Localized Surface Plasmons are non-propagating excitations of the conduction electrons of metallic nanostructures coupled to the electromagnetic field. These modes naturally generate an oscillating electromagnetic field from the scattering problem of a small, sub-wavelength conductive nanoparticle. As a result, a resonance arises, leading to field amplification on both inside and in the near-field zone outside the particle. This resonance is called localized surface plasmon resonance.

The advantages of LSPR over SPR include:

- High molecular sensitivity
- Simplicity of instrumentation
- Cost effectiveness

For gold and silver nanoparticles, the resonance falls into the visible range of the electromagnetic spectrum. It is solely because of this that the bright colors are displayed by particles both in transmitted and reflected light, due to resonantly improved absorption and scattering. This application has made itself very useful for many centuries, for example, in the staining of glass in windows or ornamental cups.

3. Optical Plasmonic Nanoantennas

3.1 What are nanoantennas?

Nanoantennas for visible and infrared radiation can strongly enhance the interaction of light with nanoscale matter by their ability to efficiently link propagating and spatially localized optical fields. This ability unlocks an enormous potential for applications ranging from nanoscale optical microscopy and spectroscopy over solar energy conversion, integrated optical nanocircuitry, optoelectronics and density-of-states engineering to ultra-sensing as well as enhancement of optical nonlinearities [47]. In particular, we discuss the role of Plasmonic resonances on the performance of nanoantennas and address the influence of geometrical parameters imposed by nanofabrication. Finally, we give a brief account of the current status of the field and the major established and emerging lines of investigation in this vivid area of research.

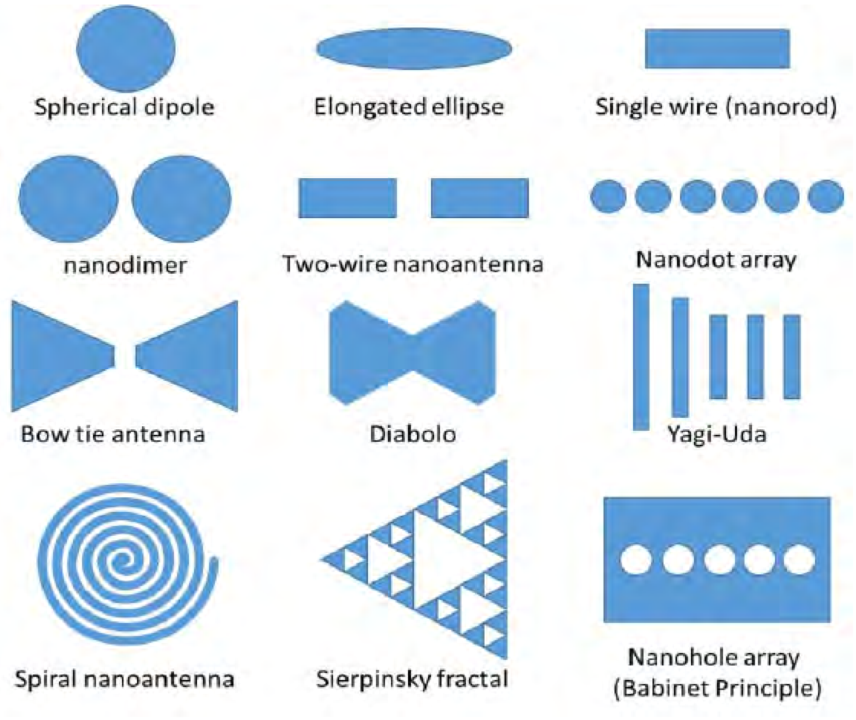

Fig 3.1 Different Plasmonic Nanoantennas

Nano antennas are used in the visible and infrared range of light. Recently, there has been a surge of research work on nanoantennas driven by their applications in areas as optical microscopy, spectroscopy, optical tweezing, and material sensing and in optical wireless integrated circuits [48]. In its simplest form, a nanoantenna is made of a rare metal rod, such as gold or silver that is embedded in a dielectric substrate. The gold or silver does not act as a good conductor at the optical range, but rather as a lossy dielectric with negative real part permittivity. When excited by a plane wave, the nanoantenna shows field enhancement and confinement in a sub wavelength region near the rod terminals or in the gap region of a dipole nanoantenna. [49]The longitudinal wavelength on the nanoantenna is considerably shorter than the free space wavelength. The field enhancement at the nanoantenna gap, in the order of hundreds relative to the incident field, attains maximum level at some resonant frequency. The latter is a sensitive function of the substrate relative permittivity**.** A physical model of bowtie nanoantenna that predicts its properties is developed and tested against simulations.

3.1.1 Plasmonic nanoantennas

Although silver and gold are the most commonly used materials, LSPR is theoretically possible in any metal, alloy or semiconductor with a large negative real dielectric constant and small imaginary dielectric constant [50]

The promise of LSPR sensors for measuring molecular concentrations binding kinetics, dye absorbance spectra and conformational changes has now been firmly established. However, transforming these early sensor designs into robust, practical tools for a wider community is an important challenge that requires the development of uniform, well characterized, highly stable substrates and instruments. A few recent examples are presented to highlight how these goals are being pursued.

Because LSPR-based sensors are by design very sensitive to changes in the characteristics of nanoparticles, uniformity in nanoparticle size, shape and composition improve sensitivity and reliability [51]. Uniform nanoparticles can be produced by using various techniques including nanosphere lithography.

In addition to uniformity, it is also important to develop sensors that are stable against solvent annealing and photo thermal annealing if high laser intensities are used. To overcome these issues, particles can be pretreated in ethanol, water and bovine serum albumin to pre-anneal them. The nanoparticles can also be protected by using controlled surface chemistries or by encapsulating them in inert layers such as silica or alumina. These surface chemistries stabilize the sensing platform and provide different affinities, permitting the detection of a wider variety of analytes.

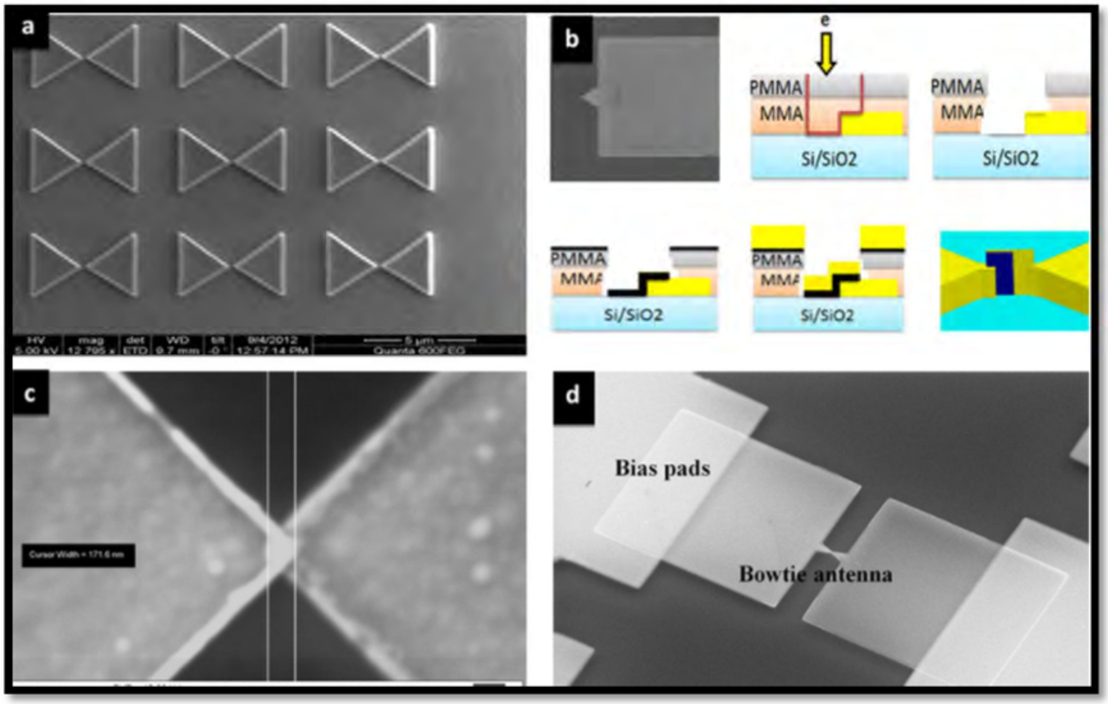

Fig 3.2 Nano antenna fabrication

The figure above shows (a) SEM image of the nanoantenna array fabricated using EBL. (b) Overlap fabrication process: (i) First antenna arm, (ii) Second arm exposure using EBL, (iii) Removing the exposed resist using a mixture of MIBK and IPA developer with ratio of 1:3, (iv) Deposition of 0.7 nm of oxide using atomic layer deposition (ALD), (v) Second arm sputtering, (vi) Complete device after the liftoff process using acetone. (c) SEM image of the fabricated overlap. (d) SEM image of the antenna-integrated diode.

Although some molecules can be detected on bare nanoparticle arrays and bare FONs, many important analytes, such as glucose, have a low affinity for the bare metal surface. In addition, oxidation of the metal surface can limit sensor stability and shelf life. Furthermore, bare nanoparticle surfaces offer limited possibilities for isolating the analyte from complex mixtures. To overcome these limitations, several methods have been used to functionalize substrates for improved affinity and selectivity. Detection is usually facilitated by the use of various coatings ranging from simple alkanes to complex macrocyclic molecules. These molecules are anchored to the noble-metal surface by a thiol group and form a SAM.[52] The SAMs serve many functions including stabilizing the nanoparticles, preventing non-specific binding, selectively binding the analyte of interest, and bringing the analyte to within a few nanometers of the nanostructure surface. In addition, antibodies can be immobilized on the SAM to facilitate protein detection.

Research is also being conducted to find alternative surface chemistries to thiol-based SAMs, which often rearrange over timescales ranging from hours to months, and suffer defects due to thermal desorption and photo oxidation. One method entails encapsulating the nanoparticles in a conformal layer of alumina or titania by using either atomic layer deposition or solution-phase sol–gel deposition. This technique protects the nanoparticle from annealing and broadens the scope of LSPR-based sensors by offering new chemical functionalities. For example, alumina selectively adsorbs polar compounds and is extremely stable against oxidation and high temperatures. [53] Recently, alumina-functionalized AgFON substrates have been used in the quantitative detection of an anthrax biomarker, calcium dipicolinate. The alumina platform also markedly increased the shelf-life of the SERS sensor (more than a year at last count). The alumina layer can be further functionalized with self-assembled monolayers by using carboxylic-acid-terminated group's andsilane chemistry. [54]

3.2 Biosensors

Biosensors are analytical devices that convert a biological response into an electrical signal. The sensing biological elements are biometric components that interact to recognize and analyze the study and the components like tissue, microorganisms, antibodies, nucleic acids and etc. Quintessentially biosensors must be highly specific, independent of physical parameters such as pH and temperature and should be reusable.

Nowadays there are many industries have a vast use of biosensors and each of them needs various types of biosensors such as enzyme-based, tissue-based, immunosensors, DNA biosensors, thermal and piezoelectric biosensors.

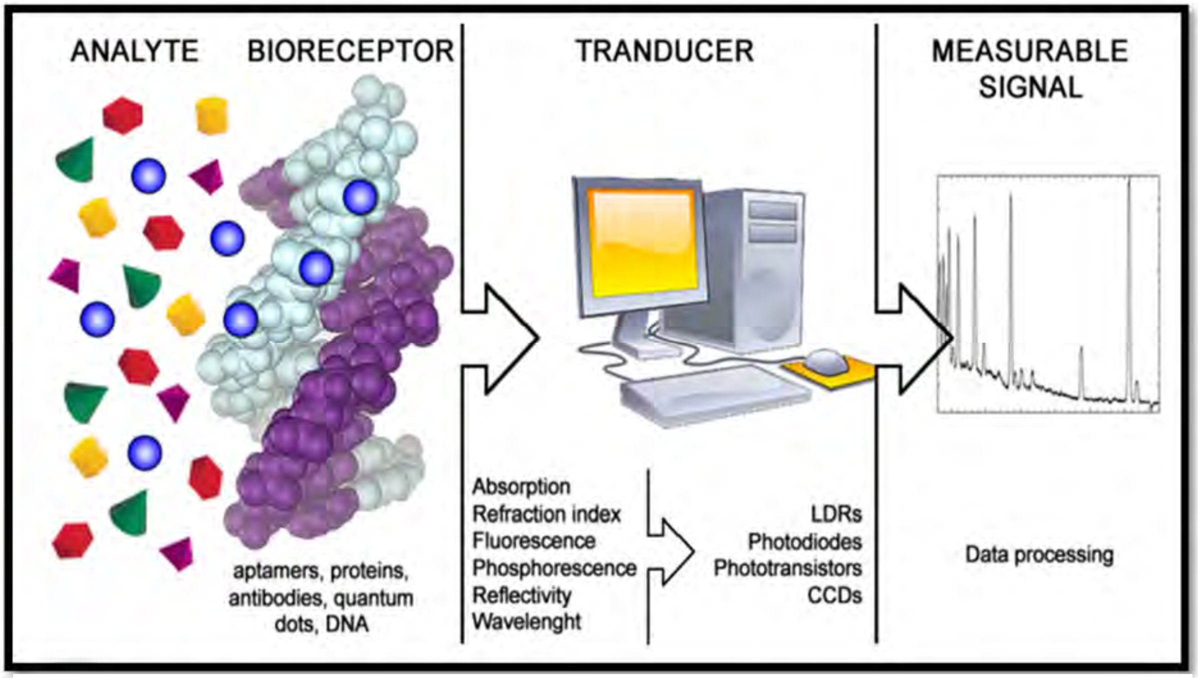

Fig 3.3 Working principle of biosensing

The first enzyme-based sensor was reported by Updike and Hicks in 1967. Enzyme biosensors have been devised on immobilization methods, i.e. adsorption of enzymes by van der Waals forces, ionic bonding or covalent bonding. The commonly used enzymes for this purpose are oxidoreductases, polyphenol oxidases, peroxidases, and amino oxidases. [55]

3.2.1 Applications of biosensors

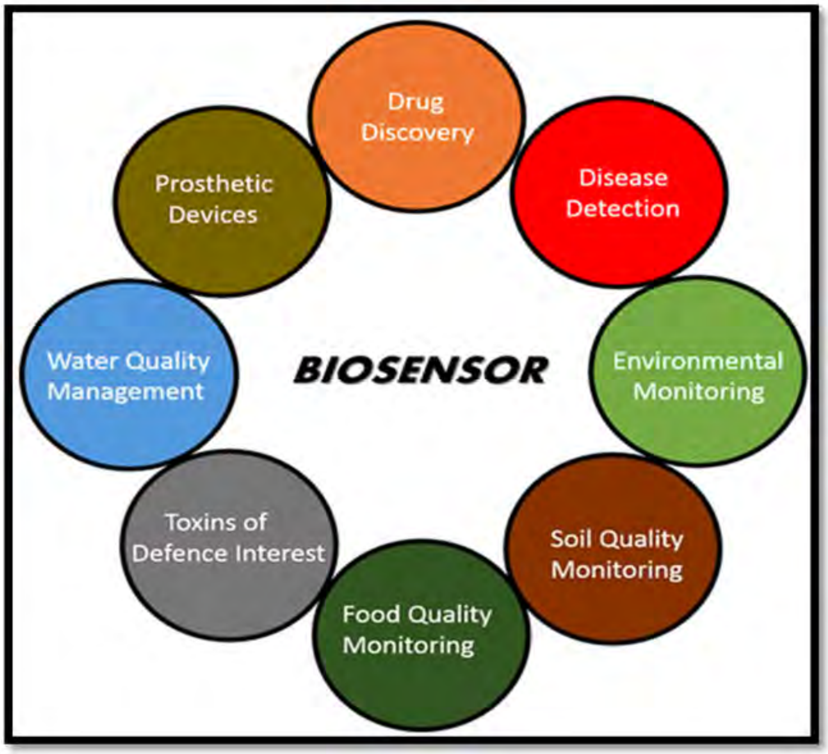

Fig 3.4 Major areas of biosensor applications

Biosensors are devices comprising a biological element and a physiochemical detector that are used to detect analytes. These instruments have a wide range of applications ranging from clinical through to environmental and agricultural. The devices are also used in the food industry.

Biosensors can provide cost-effective, easy-to-use, sensitive and highly accurate detection devices in a variety of research and commercial applications. Some examples of these applications are described below. [58]

Some examples of the fields that use biosensor technology include:

- General healthcare monitoring
- Screening for disease
- Clinical analysis and diagnosis of disease
- Veterinary and agricultural applications
- Industrial processing and monitoring
- Environmental pollution control

3.2.2 Optical nanoantennas as biosensor

For twenty years, broad research has been done in the field of biosensors for their substantial uses, such as in detection of DNA, different types of cancer and biomolecules. Therefore, an evolving technology in present biosensor research is optical antennas for label-free and real-time molecular recognition. Nowadays, numerous researchers are studying making bio-sensing optical nanoantennas. As optical antennas are governed by the rule of plasmonic, these studies are divided into two different types, according to the surface plasmons involved: (i) Surface plasmon resonance (SPR) biosensors and (ii) Localized surface Plasmon resonance (LSPR) biosensors. Surface plasmon polaritons (SPP) are the basis of SPR biosensors. SPR is a charge-density oscillation of SPP that might present at the interface of two media with dielectric constants of opposite signs, for example, a metal and a dielectric. The charge density wave is associated with an electromagnetic wave, the field vectors of which attain their maxima at the interface and decay evanescently into both media. The simplest and low cost SPR configuration is the Kretschmann configuration .Although SPR biosensors offer very high sensitivity, they are not adequate for small biomolecules in low concentrations. Recently, a new modulation technique has been employed, which surpasses the sensitivity of the standard SPR sensor. Therefore, these types of biosensors must be improved for practical use. [61]

Medical field applications

In biosensing the major application is the detection of small molecules. As bioreceptors (e.g., enzymes, antigens and antibodies) have dimensions in the range of 2–20 nm, similar to those of nanostructures, the two can be considered structurally consistent. This dimensional compatibility means that highly miniaturized signal transducers can be achieved through the combination of nanostructure characteristics, a wide selection of available bioreceptors and the rapid development of surface biofunctionalisation strategies [63].

DNA hybridization has been successfully detected by LSPR. Endo et al. [64] also monitored peptide nucleic acid (PNA)-DNA hybridization using a gold-capped nanostructure layer substrate. The optical properties of the substrate were characterized through transmission measurements, achieving target DNA detection of concentrations as low as 1 fM.

Diabetes, a disease where 80% of related deaths occur in developing countries [65] and Insulin is one of the most important indicators for diabetes diagnosis. A novel polydimethylsiloxane (PDMS) microfluidic LSPR chip has been proposed to interrogate antibody-antigen reactions in real time with the chip Biosensors 2014, 4 178 later used to detect insulin levels in the real-time monitoring of insulin and anti-insulin antibody immunoreactions with a 100 ng/mL detection limit [66].

Ultra-sensitive influenza detection through antigen-antibody interaction on a gold surface was successfully shown using LSPR [67]. In this work, an active immobilization method was developed to facilitate the biosensing of avian influenza virus. The gold binding polypeptide (GBP)-fusion protein was bound onto the gold substrates by means of specific interaction. The GBP-fusion method allows the immobilization of proteins in bioactive forms onto the gold surface without surface modification. This methodology could be extended to provide the detection of clinical diseases and other protein-protein interactions.

Salmonella presents both a threat to public health and the risk of significant economic losses. In developing countries, nosocomial outbreaks are more prevalent, but the combination of increased agricultural activity and poor water quality is likely to increase the risks of foodborne Salmonella. The detection of bacterial pathogens remains challenging [68], with difficulties in repeatedly detecting the levels to an acceptable accuracy, and this is no different for LSPR-based detection [69]. More recently, the simultaneous detection of tuberculosis and Schistosoma japonicum (a parasite that affects around 210 million people worldwide, especially in Asian, African and Latin-American countries) using a simply fabricated substrate has been demonstrated in low serum concentrations (1:10,000) without the need for sample processing [70]. This marks a significant step in the detection of pathogens. A research propose a highly sensitive LSPR immunosensor for the detection of the HIV-1 virus. The surface of the Au nanostructure was modified with HIV-1 antibody fragments to measure various concentrations of HIV-1 particles quantitatively with a 200 fg/mL detection limit. Since this LSPR Biosensors 2014, 4 179 immunosensor has the advantages of rapid preparation, high sensitivity and selectivity, it is a promising approach for the screening of other viral particles. [71]

The evaluation of cholesterol concentrations of the lipid membrane could be useful for the early detection of heart diseases and cancer. High levels of cholesterol in the lipid membrane can be associated with the initial formation of tumours, with two examples being breast and prostate cancer. A device based on LSPR has been proposed and simulated with FullWAVETM to measure cholesterol in the lipid membrane [72].

LSPR-based biosensors could also be used for the diagnosis of pregnancy-related conditions, such as preeclampsia, a hypertensive disorder occurring during pregnancy. Uric acid in urine caused by proteinuria can be used as a biomarker for preeclampsia, with concentrations above 0.4 mM being indicative of severe preeclampsia [73]. With 99% of the 500,000 maternal deaths each year occurring in developing countries and preeclampsia being one of the leading causes of maternal death worldwide, the sensitivity offered by an LSPR platform could allow for the early detection of such conditions, where early medical treatment could alter the course of progression.

As mentioned above LSPR sensors can be designed to detect a variety of biological and pathogenic molecules, making them a valuable diagnostic tool for the biomedical industry. Now, we will describe one of the most important biological applications of the LSPR biosensor to date, namely the detection and diagnosis of a possible biomarker for Alzheimer's disease. One hallmark of Alzheimer's disease is the formation of insoluble protein deposits, known as amyloid plaques, in brain tissue. These plaques are formed from the soluble precursor amyloid beta, a small 39- to 43-amino acid protein that is present in elevated levels in the brain and cerebral spinal fluid (CSF) of Alzheimer's disease sufferers [59]. Single units of amyloid beta readily assemble into oligomers of two to 24 units (sometimes referred to as amyloid-b-diffusible ligands, or ADDLs), and these oligomers themselves exhibit significant neuronal toxicity [74]. Though not proven, it is increasingly likely that ADDLs may cause early memory loss in Alzheimer's disease [75, 76].

Currently, the diagnosis of Alzheimer's disease is made based on symptomatic evidence, there being no diagnostic method based on the molecular pathology of the disease currently available. The LSPR sensor, however, represents a promising step towards the molecular detection of the ADDL biomarker. Antibodies which specifically recognize amyloid beta oligomers were covalently attached to a chemical monolayer on an NSL-fabricated NP surface. Subsequently, CSF from patients diagnosed with Alzheimer's disease or from healthy, age-matched controls was flowed over the sensor surface .Any amyloid beta oligomers that remained bound to the antibody-functionalized surface were detected using a second capping antibody , thus completing the ''sandwich'' assay. By measuring extinction shifts in response to the addition of capping antibody, it was shown that diseased patients had significantly higher concentrations of amyloid beta oligomers than did age-matched controls The experiment was repeated using soluble post-mortem brain extract from diseased and control patients, with similar results The results from this study not only confirmed the relationship between elevated amyloid beta levels and Alzheimer's disease, but also suggested that the LSPR sensor could be used as an early detection technique for the condition. Moreover, the sandwich assay described above is broadly generalizable, suggesting that the LSPR sensors might have applications for other biosensing applications.

Medical-orientated LSPR biosensors are expected to evolve mainly in the following directions

- higher sensitivity;
- detection of more complex systems beyond the molecular level, such as cellular-, intracellular- and tissue-level detection;

- a combination of current nanostructures with other materials;
- a combination of LSPR with other available transduction methods;
- overcoming the challenges of using LSPR sensing at the point of care and in field applications.

Agriculture and Environmental Monitoring

Currently, around one billion people suffer from severe hunger, and this malnutrition makes people more susceptible to illness, poor growth and reduced work capacity, all leading to a depressed economy. Thus, food and agriculture can also be considered intrinsically linked with poverty. With increasing population, changes in the climate and diminishing natural resources, agricultural productivity has again been put under severe strain. With the development of affordable biosensing technologies, agricultural output could be both increased and made more sustainable by improving the use of soil, water and fertilizer, as well as crop resistance to disease.[82] Sustainability will come from better education, as well as the ability to monitor the environment for contaminants and pollutants in order to improve agricultural techniques. The ability to monitor plant nutrients allows the yield and quality of crops to be improved. The current methods of analyzing plant nutrients include: inductively-coupled plasma atomic emission spectroscopy (ICP/AES), X-ray fluorescence spectrometry (XRF), inductively-coupled plasma mass spectrometry (ICP-MS) and atomic absorption spectrometry (AAS), but all require the device to be situated in laboratory environments, due to several constraints, such as size, cooling and necessary gas supplies. LSPR has been shown to offer enhanced sensitivity and limits of detection (LOD) for the laser-induced breakdown spectroscopy (LIBS) detection of calcium, iron, copper, sodium, potassium, cobalt, manganese and molybdenum. [77] This quick and simple technique highlights the power of an LSPR-based sensor for this application.

Agriculture is the single largest user of surface water and is both a cause and a victim of water pollution (quality) and contamination (health risk). Therefore the production/processing/distribution chain requires careful screening to allow pollutant/contaminant detection and the determination of the likely source. Endocrine disrupting chemicals (EDCs), such as dioxins, industrial chemicals (e.g., PCBs (polychlorinated biphenyls), agrochemicals (e.g., atrazine) and pharmaceuticals all accumulate in vivo, causing abnormalities in growth, reproduction, development, behavior, immune response and the development of malignant tumors. Rapid screening for EDCs is highly needed. The detection of dioxins, PCBs and atrazine have been demonstrated using competitive and sandwich immunoassays [78]; PCBs have also been measured to the ppb level (50 pM) through LSPR combined with SERS [79]. Organophosphate (OP) pesticides pose a hazard to human health (eye pain, abdominal pain, paralysis and respiratory failure) and, as such, are an important target for detection. LSPR detection of OP agents at 0.234 ppb LOD has been demonstrated by covalently coupling acetylcholinesterase (AChE) to nanostructures. OPs irreversibly bind with AChE, an essential enzyme in nerve impulse responses that causes OP's toxicity. The detection of chlorpyrifos and malathion, pesticides predominantly found in surface waters of developing countries, has been demonstrated to the ppb level using a simple UV-Vis spectrometer· [81] The use of Na2SO4 improved the aggregation of the gold nanostructures, allowing amplified LSPR spectral shifts to be observed at low concentrations. Mercury detection has been achieved by monitoring the affinity difference of Hg and Au nanostructures with DNA; increased concentrations of Hg cause changes in the aggregation state of Au nanostructures, and this yields stronger LSPR intensities. This work is of significant importance given that concentrations of the majority of metals, regardless of being essential or non-essential, are toxic for living cells· [83]

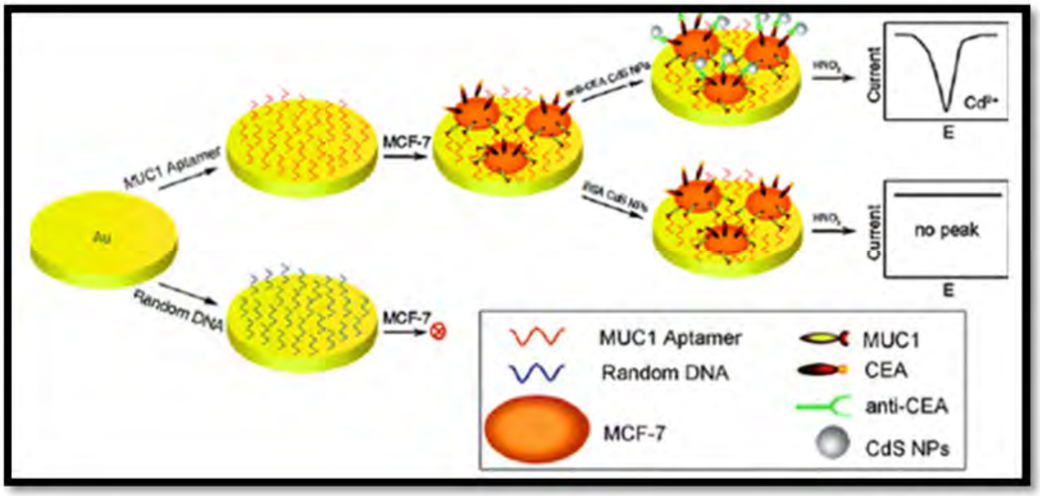

Fig 3.5 Detection of cancer cells

3.3 Protein as bimolecular analyte

Proteins are the most diverse biomolecules on Earth, performing many functions required for life. Protein enzymes are biological catalysts, maintaining life by regulating where and when cellular reactions occur. Structural proteins provide internal and external support to protect and maintain cell shape. For example, keratins are an important class of structural proteins found in the hair, skin, nails, and feathers of animals. Motility proteins provide the basis for cellular and whole organism movement, including muscle motor proteins that can move entire animals! Membrane proteins transmit signals during cell-to-cell communication, transport molecules into and out of cells, and protect living organisms by identifying and flagging invaders. [61]

Protein functions are so diverse because of the many unique three-dimensional structures protein polymers form. Despite such variety, proteins also share several specific structural characteristics in their monomers, the amino acids. Structural similarities among amino acids make protein synthesis a uniform and regulated process; however, each amino acid contains a unique structural component as well. Specific differences between each amino acid interact to create unique three-dimensional protein structures. Combined, the similarities and differences between amino acids explain how cells can build a diverse pool of proteins from the same set of building blocks.

The biomolecules or proteins are used for the thesis is given below [66]:

Protein	Shape	Major Axis Dimension	Minor Axis-1 Dimension	Minor Axis-2 Dimension	Mass(kDa)	Refractive Index, n
Lysozyme (Lys)	Ellipsoid	4.5	1.8	1.8	14.3	1.50
Human Serum Albumin (HAS)	Ellipsoid	7.5	6.5	4	66.4	1.44
Fibrinogen (Fb)	Elongated ellipsoid	46	6	3	390	1.39

3.3.1 Lysozyme

Lysozyme (1, 4-β-N-acetylmuramidase) is an enzyme that plays an important role in the prevention of bacterial infections. It does this by attacking a specific component of certain bacterial cell walls, peptidoglycan. Peptidoglycan is composed of the repeating amino sugars, N-acetylglucosamine (NAG) and N-acetylmuramic acid (NAM), cross linked by peptide bridges. Lysozyme acts by hydrolyzing the bond between NAG and NAM, increasing the bacteria's permeability and causing the bacteria to burst.

Lysozyme is widely distributed in plants and animals. Human lysozyme is expressed in the mucous membranes of the nasal cavity and tear ducts. It is also found in saliva, tears, milk, cervical mucus, leukocytes, and kidney tissue. The majority of the lysozyme used in research is purified from hen egg whites.

The primary structure of lysozyme is a single polypeptide containing 129 amino acids. In physiological conditions, lysozyme is folded into a compact, globular structure with a long cleft in the protein surface. This cleft is the active site involved in binding to the bacterial carbohydrate chain and subsequently cleaving it.

Lysozyme was discovered by Alexander Fleming in 1921 when he demonstrated that his own nasal mucus had the ability to inhibit the growth of a certain strain of bacteria in culture. He realized that this was largely due to the action of a protein within the mucus that caused the bacterial cells to lyse or break apart. Hence, he named the protein lysozyme. In a 1922 publication, he reported its activity in hens' egg white, tears, saliva, sputum, and nasal secretions. In a subsequent study, Fleming in collaboration with V. D. Allison detected lysozyme in human blood serum, saliva, milk, and a wide variety of other fluids.

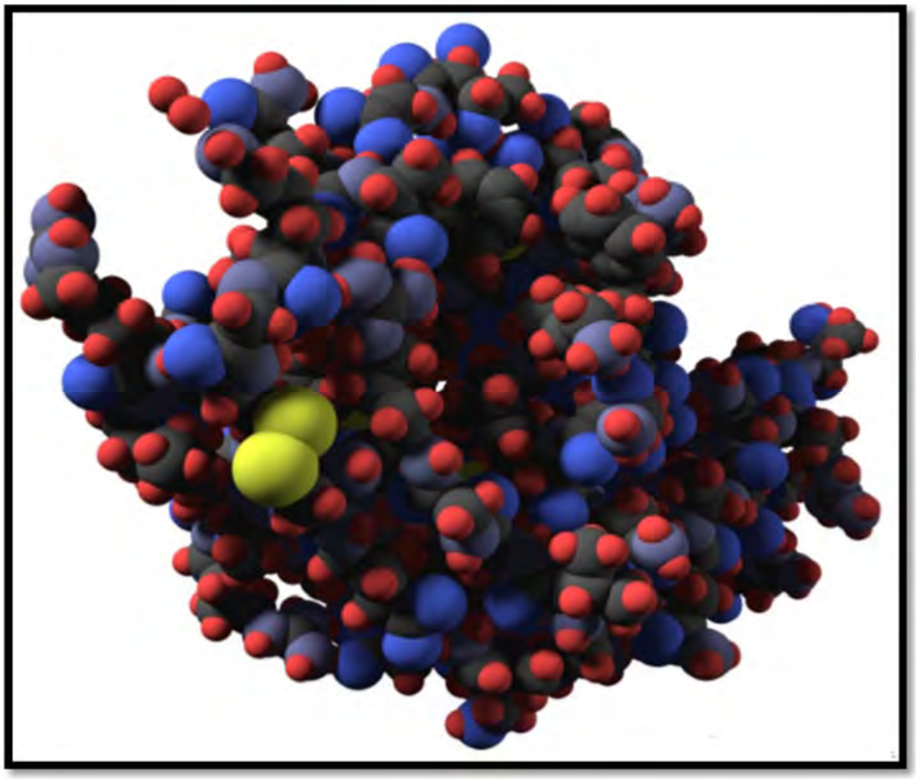

Fig 3.7 Lysozyme structure

Despite lysozyme's antimicrobial activity toward harmless, airborne bacteria, it proved to be ineffective against disease causing bacteria. Fleming, realizing that there were no broad medical applications to his discovery, moved on to other studies in chemical antiseptics. However, his work on lysozyme further stimulated Fleming's interest in antimicrobial agents and consequently led to the discovery of penicillin in 1928, for which he later received a Nobel Prize in 1945.

In 1966, David Chilton Phillips, using x-ray crystallography, determined lysozyme's structure, the first ever solved for an enzyme. From this work, Phillips was able to explain the mechanism of the enzyme's catalytic activity. Lysozyme is now one of the most abundant protein structures in the Protein Data Bank. [62]

3.3.2 Human Serum Albumin (HSA)

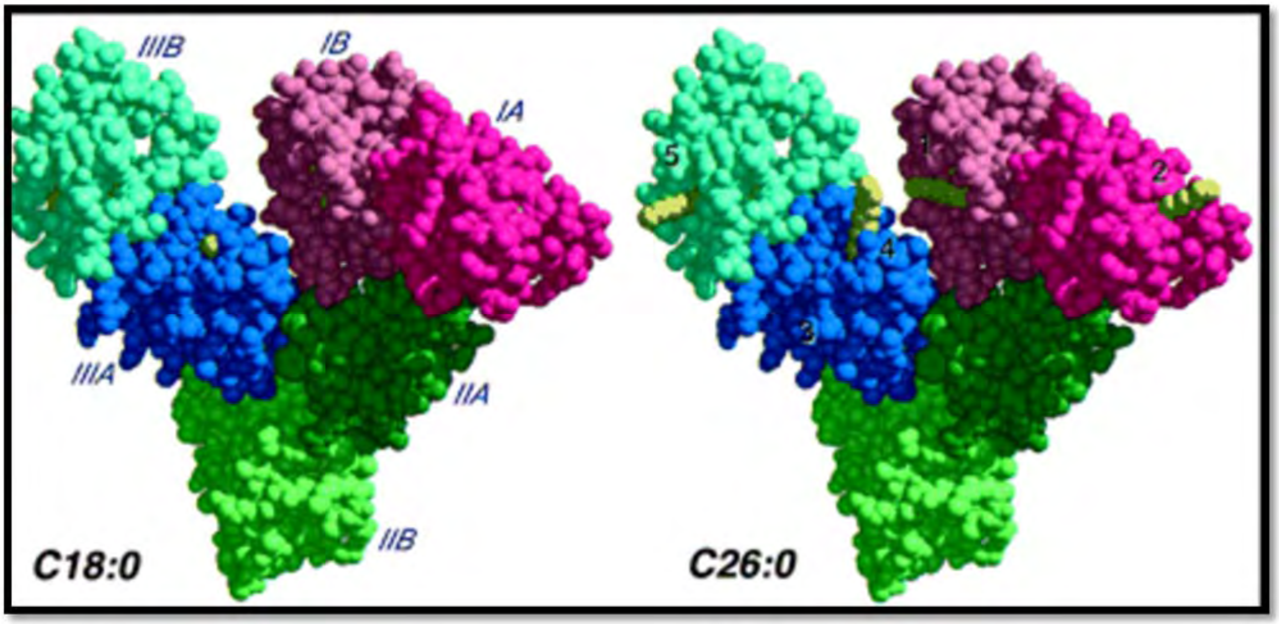

Fig 3.8 HSA structure

Human serum albumin is the serum albumin found in human blood. It is the most abundant protein in human blood plasma; it constitutes about half of serum protein. It is produced in the liver. It is soluble and monomeric.

Albumin transports hormones, fatty acids, and other compounds, buffers pH, and maintains oncotic pressure, among other functions.

Albumin is synthesized in the liver as preproalbumin, which has an N-terminal peptide that is removed before the nascent protein is released from the rough endoplasmic reticulum. The product, ovalbumin, is in turn cleaved in the Golgi vesicles to produce the secreted albumin.

The reference range for albumin concentrations in serum is approximately 35 - 50 g/L (3.5 - 5.0 g/dL).[1] It has a serum half-life of approximately 20 days. It has a molecular mass of 66.5 kDa.

The gene for albumin is located on chromosome 4 and mutations in this gene can result in anomalous proteins. The human albumin gene is 16,961 nucleotides long from the putative 'cap' site to the first poly (A) addition site. It is split into 15 exons that are symmetrically placed within the 3 domains thought to have arisen by triplication of a single primordial domain. [63]

Its functions include:

- Maintains oncotic pressure
- Transports thyroid hormones
- Transports other hormones, in particular, ones that are fat-soluble
- Transports fatty acids ("free" fatty acids) to the liver and to myocytes for utilization of energy
- Transports unconjugated bilirubin
- Transports many drugs; serum albumin levels can affect the half-life of drugs
- Competitively binds calcium ions (Ca^{2+})
- Serum albumin, as a negative acute-phase protein, is down-regulated in inflammatory states. As such, it is not a valid marker of nutritional status; rather, it is a marker of an inflammatory state
- Prevents photo degradation of folic acid

3.3.3 Fibrinogen

Fibrinogen (factor I) is a glycoprotein in vertebrates that helps in the formation of blood clots. It consists of a linear array of three nodules held together by a very thin thread which is estimated to have a diameter between 8 and 15 Angstrom (Å). The two end nodules are alike but the center one is slightly smaller. Measurements of shadow lengths indicate that nodule diameters are in the range 50 to 70 Å. The length of the dried molecule is 475 ± 25 Å. The fibrinogen molecule is a soluble, large, and complex 340 kDa plasma glycoprotein, which is converted by thrombin into fibrin during blood clot formation. It has a rod-like shape with dimensions of 9 × 47.5 × 6 nm and it shows a negative net charge at physiological pH (IP at pH 5.2). Fibrinogen is synthesized in the liver by the hepatocytes. The concentration of fibrinogen in the blood plasma is 200–400 mg/dL (normally measured using the Claus method). During normal blood coagulation, a coagulation cascade activates the zymogen prothrombin by converting it into the serine protease thrombin. Thrombin then converts the soluble fibrinogen into insoluble fibrin strands. These strands are then cross-linked by factor XIII to form a blood clot. FXIIIa stabilizes fibrin further by incorporation of the fibrinolysis inhibitors alpha-2antiplasmin and TAFI (thrombin activatable fibrinolysis inhibitor, procarboxypeptidase B), and binding to several adhesive proteins of various cells. Both the activation of factor XIII by thrombin and plasminogen activator (t-PA) are catalyzed by fibrin. Fibrin specifically binds the activated coagulation factors factor Xa and thrombin and entraps them in the network of fibers, thus functioning as a temporary inhibitor of these enzymes, which stay active and can be released during fibrinolysis. Research from 2011 has shown that fibrin plays a key role in the inflammatory response and development of rheumatoid arthritis. [64]

The usefulness of fibrinogen as a marker of inflammation, trauma and various types of infections have been reported in a number of scientific papers

- General inflammatory response due to an infection: Fibrinogen normally increases within 24 to 48 hours from a normal level of 2-4 g/L and may exceed 10 g/l on day 4 - 7 post infection. It is not uncommon in horses to have increased plasma fibrinogen levels as the sole indicator of inflammation.
- Surgical trauma: Levels of serum amyloid A, fibrinogen and iron reflect the intensity of the surgical trauma, whereas WBC do not do this. Fibrinogen is therefore a good diagnostic marker to monitor the healing process after a surgical procedure.

- Bacterial infection: The fibrinogen level can be used to predict the time course of a bacterial infection as has been shown with Escherichia coli endotoxin. It has also been shown to be an effective screening tool to diagnose RhodococcusEqui infections in foals. Fibrinogen concentrations has also been shown to enable a more precise diagnosis of the severity of an inflammation.

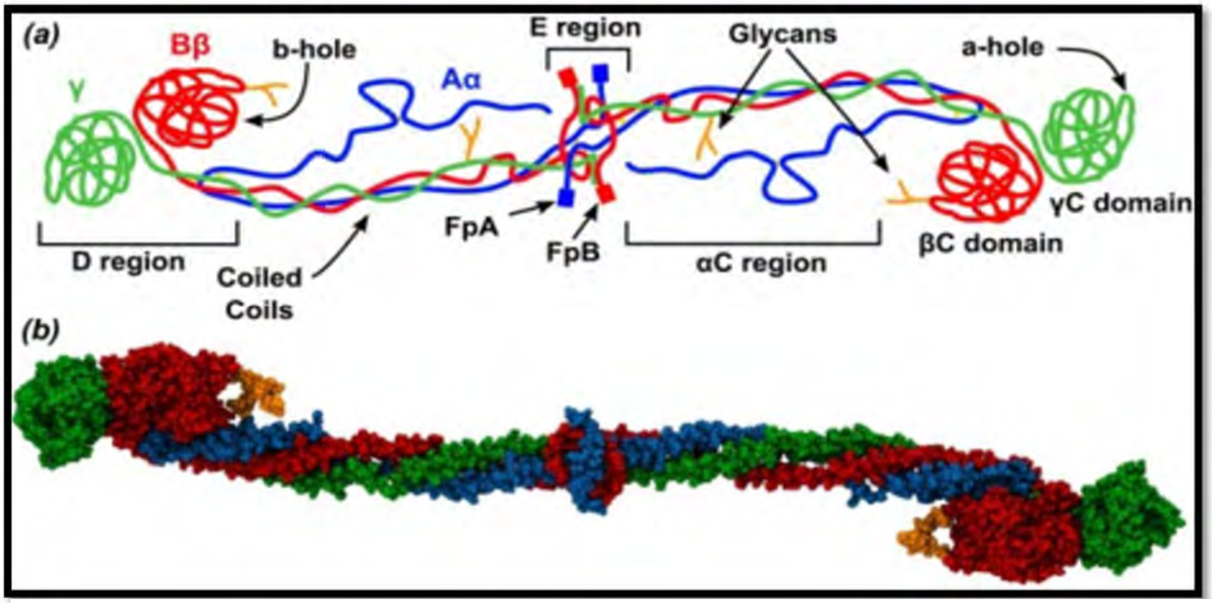

Fig 3.9 Fibrinogen structure

Fig 3.9 shows the fibrinogen molecule. Of which, (a) is a schematic representation of the fibrinogen molecule and (b)is Van der Waal's representation of the structure.

- Viral infection: Horses with equine influenza and herpes virus 2 has been proven to show elevated fibrinogen levels 3 days post infection.
- Parasite infection: Parasitized (Strongelus Vulgaris) ponies showed in a study to have significantly elevated fibrinogen levels compared to a control group 9, 14, 21 and 45 days after infection. Heidmann
- Aseptic arthritis: Experimentally induced aseptically inflammation showed a significant increase in fibrinogen with a maximum level 3 - 6 days post-injections

3.4 Summary

Main elements of biomolecules are carbon and hydrogen with nitrogen, oxygen, sulphur and phosphorus. These biomolecules has a universal name which is biological material. In the sector of biology and biochemistry, biomolecules and their reactions are considered for research and analysis. These molecules are consists of hydrogen, carbon, nitrogen, oxygen and sulfur.

.Lysozyme is a special type of enzyme which can be found in salvia, sweat, breast milk, tears and other type of body fluids. It is also found in egg white. It mainly works as antibacterial enzyme. Lysozyme is capable of destroying the growth of bacteria. Carbohydrate and Peptidoglycan layer are the elements which are present in the cell walls of bacteria and lysozyme breaks down the elements, in this way it can stop the growth of bacteria. It catalyzes the hydrolysis of 1, 4-β linkages between N-acetylmuramic acid and N-acetyl-D-glucosamine.

Serum albumin present in human blood is said to be the human serum albumin. This serum is soluble, monomeric and produced in liver. It is a globular protein of 585 amino acids. The amount of HSA in blood is the almost 60% of the total protein present in blood serum. Albumin is synthesized in the liver as preproalbumin which has an N-terminal peptide that is removed before the nascent protein is released from the rough endoplasmic reticulum.

Fibrinogen (*factor I*) is a glycoprotein in vertebrates that helps in the formation of blood clots. It consists of a linear array of three nodules held together by a very thin thread which is estimated to have a diameter between 8 and 15 Angstrom (Å). The two end nodules are alike but the center one is slightly smaller. Measurements of shadow lengths indicate that nodule diameters are in the range 50 to 70 Å. The length of the dried molecule is 475 ± 25 Å.

4 Bowtie Nanoantenna

4.1 Introduction

One of the great challenges in the field of nanotechnology is optical imaging—specifically, how to design a microscope that produces high-resolution images of the nano-sized objects that researchers are trying to study. For example, a typical DNA molecule is only about three nanometers wide—so tiny that the contours of its surface are obscured by light waves, which are hundreds of nanometers long.

Now, researchers from Stanford University have greatly improved the optical mismatch between nanoscale objects and light by creating the "bowtie nanoantenna," a device 400 times smaller than the width of a human hair that can compress ordinary light waves into an intense optical spot only 20 nanometers wide. These miniature spotlights may one day allow researchers to produce the first detailed images of proteins, DNA molecules and synthetic nano-objects, such carbon nanotube bundles.

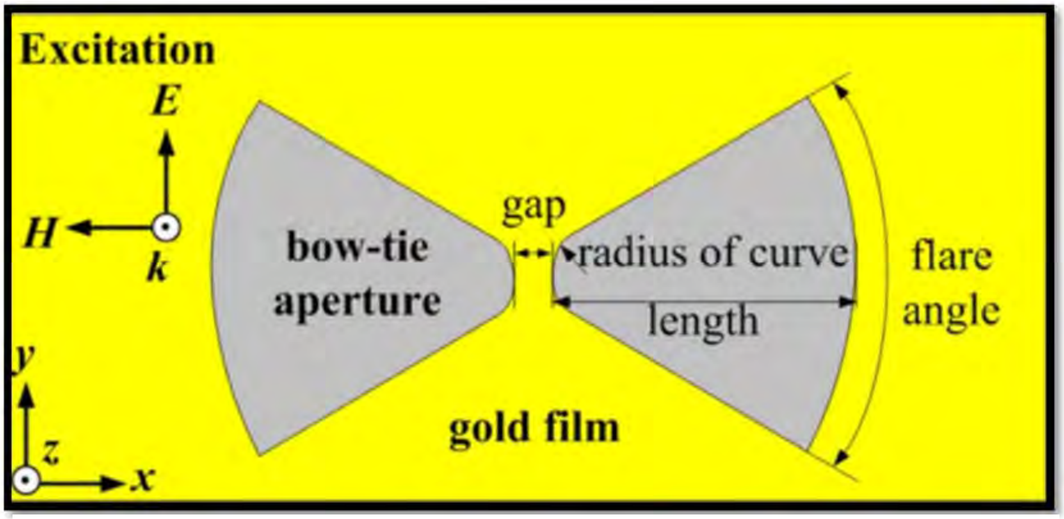

Fig 4.1 Bow tie aperture top view

.

Golden bowties: The bowtie nanoantenna consists of two triangular pieces of gold, each about 75 nanometers long, whose tips face each other in the shape of a miniature bowtie. The device operates like an antenna for a radio receiver, but instead of amplifying radio waves, the bowtie takes energy from an 830-nanometer beam of near-infrared light and squeezes it into a 20-nanometer gap that separates the two gold triangles. The result is a concentrated speck of light that is a thousand times more intense than the incoming near-infrared beam.

The influence of the geometrical parameters (antenna length, gap dimension and bow angle) on the antenna field enhancement and spectral response is important. Bowtie antennas confine the field in a volume well below the diffraction limit, defined by the gap dimensions. The enhancement can reach three orders of magnitude for the smallest examined gap. The bowtie antenna exhibits multiple resonances. Furthermore, the sensitivity of the antennas to index changes of the environment and of the substrate has been investigated in detail for biosensing applications.

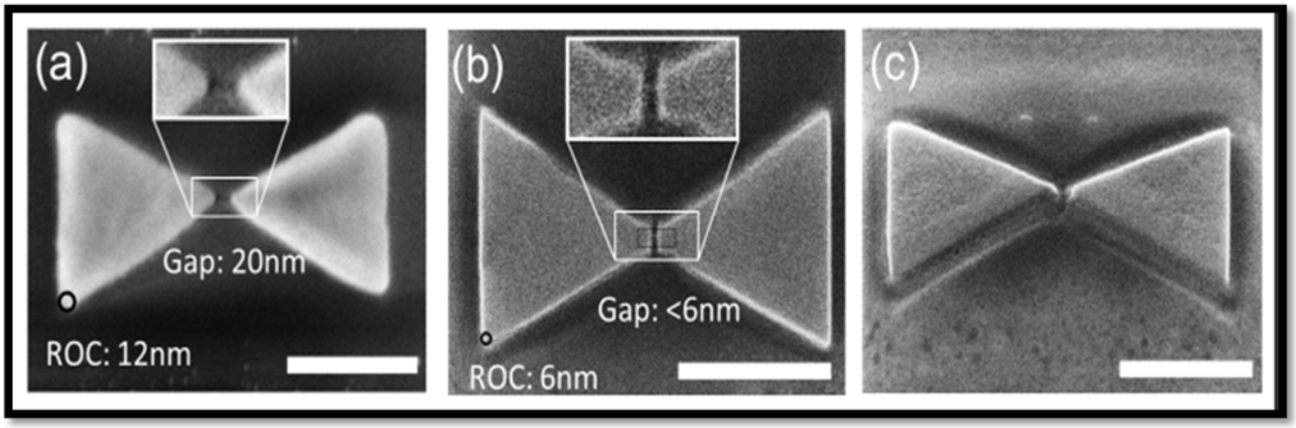

Fig4.2 SEM image of various gap sized Au bowtie

Bowties also may have applications in Raman spectroscopy, a technique that allows scientists to identify individual molecules by measuring the vibrational energy the molecule emits when exposed to light. "It's analogous to fingerprinting," Schuck explains. "Each molecule has a unique vibrational energy, and bowties have a potential use as biological or chemical sensors that can differentiate molecules."

4.2 Analyzed Structure

The localized plasmonic near-field of the bowtie nanoantennas, can be changed by modifying the nanostructure shape as well as the refractive index of the surrounding medium. Geometrical parameters such as gap size, height, bowtie angle and radius of curvature have a direct influence in the LSPR, as they change the spectral position and narrowness of the plasmonic peak in the extinction cross-section.

For the structure we analyzed, we fixed the height of the nanoparticles to 50 nm, the length of their sides to 70 nm, varying the curvature of the vertices, starting from 0 nm. The basic structure has a gap of 5 nm, which too, was varied. The nanoparticles which were modeled as equilateral triangles, is deposited on ITO / glass with a thickness of 4000 nm and a titanium adhesion layer of 3 nm of thickness was added under the gold nanoparticles, as can be observed in Fig. (), which is needed in actual applications for the gold to adhere to the SiO2 substrate. The entire structure was immersed in different solutions of varying refractive index, starting with water (n=1.33). The TFSF source with a wavelength range from 450 nm to 1000 nm was placed both parallel (TM) and perpendicular (TE) to the major axis of the structure.

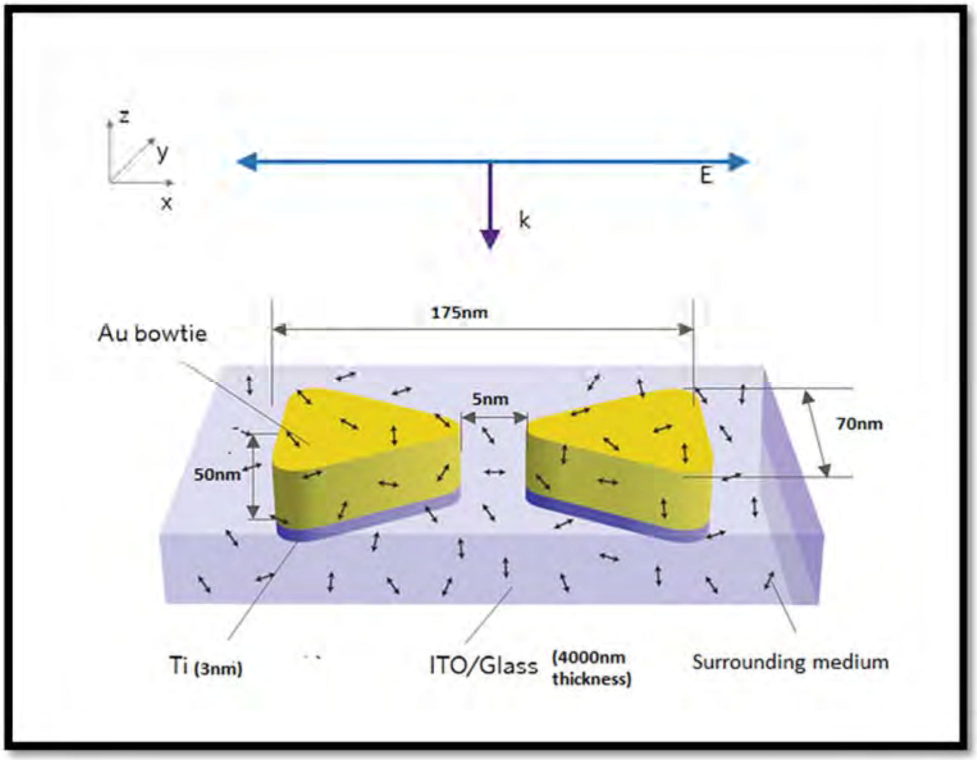

Fig 4.3 Experimental Setup

Fig 4.3 shows the experimental setup of Isolated Bowtie Structure. The presence of a metal adhesion layer induces the broadening of the LSPR and diminishes the scattering amplitude [21] and therefore the adhesion layer should be maintained as thin as possible. The choice of the substrate is very important due to the screening effect [22] and so it is convenient to choose a substrate with a refractive index as close as possible to that of the medium that surrounds the bowties.

We also analyzed a bowtie array structure, shown in fig (4.4).If the wavelength of the scattered light is close to both the pitch distances of the array and the LSPR wavelength then a dramatic modification of the extinction cross-section will arise due to a collective coupling of every localized Plasmon. We therefore performed simulations for different values of the refractive index of the medium occupying the half space above the bowtie array for EM field polarization.

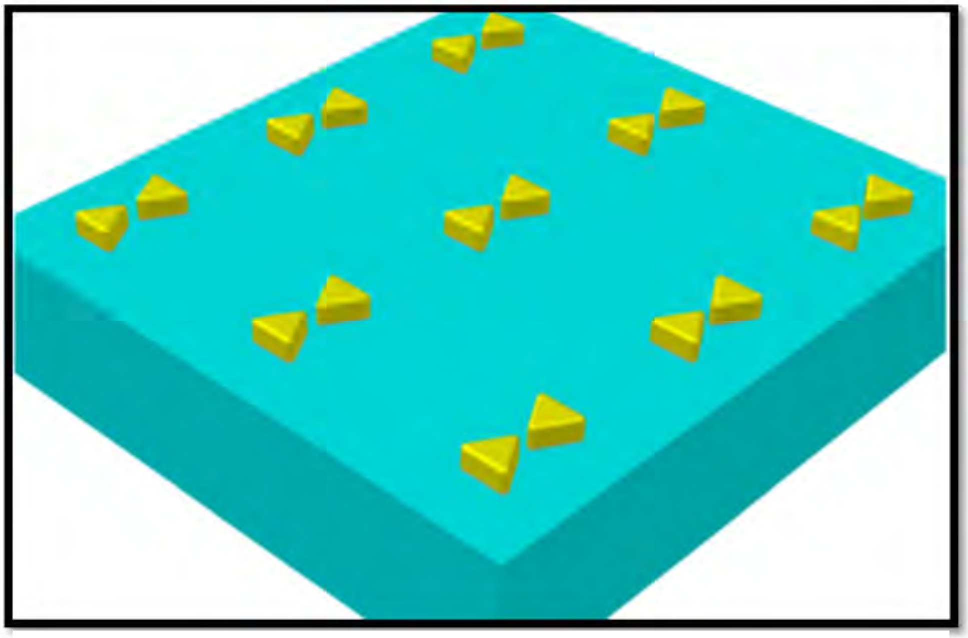

Fig 4.4 Bowtie array

5. Finite-Difference Time-Domain (FDTD) method

5.1 Introduction

The finite-difference time-domain (FDTD) method is arguably the simplest, in terms of implementation, of the full-wave techniques used to solve problems in electromagnetics. It is well suited to modeling inhomogeneous materials and simulation of wideband antennas. Since it is a time domain method, Fourier techniques are applied to convert the time domain results into the frequency domain and thus a single FDTD simulation can be used to characterize a wideband frequency response

The FDTD method uses grid-based differential numerical modeling methods which are called the finite difference methods. The time-dependent Maxwell's equations which are in partial differential form are changed into discrete forms and the resulting finite-difference equations are solved in either software or hardware. This uses the "leapfrog" method where the electric field vector components in a volume of space are solved at a given instant in time; then the magnetic field vector components in the same spatial volume are solved at the next instant in time, and the process is repeated over and over again until the desired transient or steady-state electromagnetic field behavior is fully evolved. [24]

When Maxwell's differential equations are examined, it can be seen that the change in the E-field in time (the time derivative) is dependent on the change in the H-field across space (the curl). This results in the basic FDTD time-stepping relation that, at any point in space, the updated value of the E-field in time is dependent on the stored value of the E-field and the numerical curl of the local distribution of the H-field in space. The same is observed in case of H-field. However, when multiple dimensions are considered, calculating the numerical curl can become complicated. Hence, Kane Yee's 1966 paper proposed a scheme, now known as a **Yee lattice**, which remains at the core of many current FDTD software constructs. This scheme requires that E-field updates are conducted midway during each time-step between successive H-field updates, and vice versa. [23]

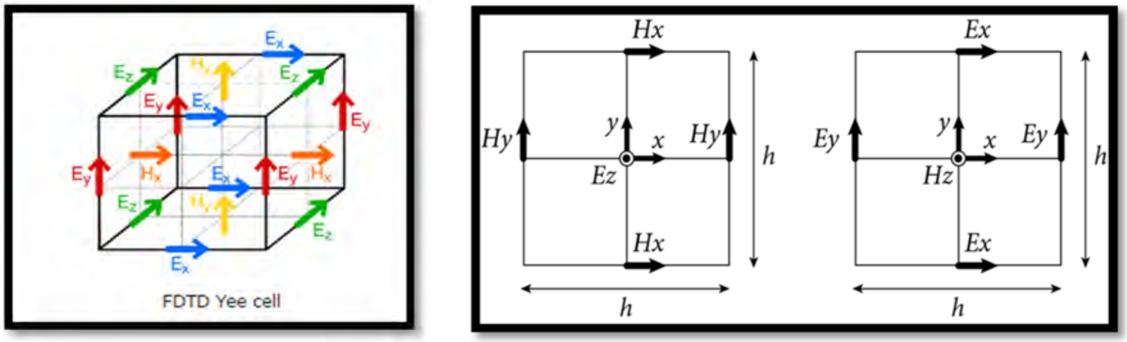

Fig 5.1 Yee cell

Fig 5.1 shows the FDTD Yee cell [25]

5.2 Lumerical Solutions: About the software

Lumerical is photonic simulation software that enables us to **understand light**, and predict how it behaves within complex structures, circuits, and systems. Using Lumerical's design tools, one can fabricate, improve and process as well as run tests without having to physically create the structures. These features allow designers check the accuracy of designs prior to manufacturing, create new product concepts, and explore long-term innovative photonics research such as quantum computing. Examples include: biomedical researchers exploring how light scatters from cancerous cells as the basis for new diagnostics; innovators modeling optical materials that store vast amounts of information more efficiently; and engineers designing high-speed communication systems that transmit information optically within datacenters and even between and within computer chips. Not only are these designers able to create better performing components, they can do so in far less time, at lower costs, and with greater accuracy. Furthermore, Lumerical's products allow optical, electrical, and thermal and circuit simulations. [26]

Fig 5.2 Lumerical Component Designs

For our purpose, we have used Lumerical's FDTD solution. Lumerical's FDTD Solutions is a 3D Maxwell solver, capable of analyzing the interaction of UV, visible, and IR radiation with complicated structures employing wavelength scale features. FDTD Solutions can be used across a wide array of nanophotonic research areas, including plasmonics, particle and surface scattering and microscopy and lithography.

5.2.1 Structure and Material Modeling

For our design of a nanoantenna of the bow-tie shape, we used two triangles from structures, which is located at the top right of the software above the object tree window. As a complete setup may contain a large number of objects, the object tree was designed to allow for organization and easy selection. It must be mentioned that one of the selected triangles was rotated in order to give the structure its desired shape. The rotation can be done with the help of the four windows in the layout, each showing a different view of the structure: xy, xz, yz and a 3D view of the design.

Next, we defined the dimensions of the model by editing its properties, where we fix the x vertices at 240 nm. It should be noted that we changed our length units to nanometer as our work involves nanostructures. The material of the polygonal structures faced tip to tip is gold (Au) of height 50nm. Between the triangles, the basic gap size was 5nm which was later varied up to 100nm. The optical properties of Au were taken from Palik's handbook.

As a substrate on which the polygonal structure would be placed, we selected the substrate material to be Glass (SiO2) of thickness 4000nm. SiO2, which is basic sand glass, exhibits several properties for which it is a suitable substrate for our simulation. It has high thermal conductivity and low moisture absorption. Furthermore, SiO2 has flexible thickness control while the costs are low as well.

An Indium Tin Oxide (ITO) layer of thickness 50nm was assumed to cover the glass substrate.

Between the Au bowtie structure and glass, a titanium (Ti) adhesion layer was placed with a thickness of 3nm. The optical properties of Ti were taken from Palik's handbook.

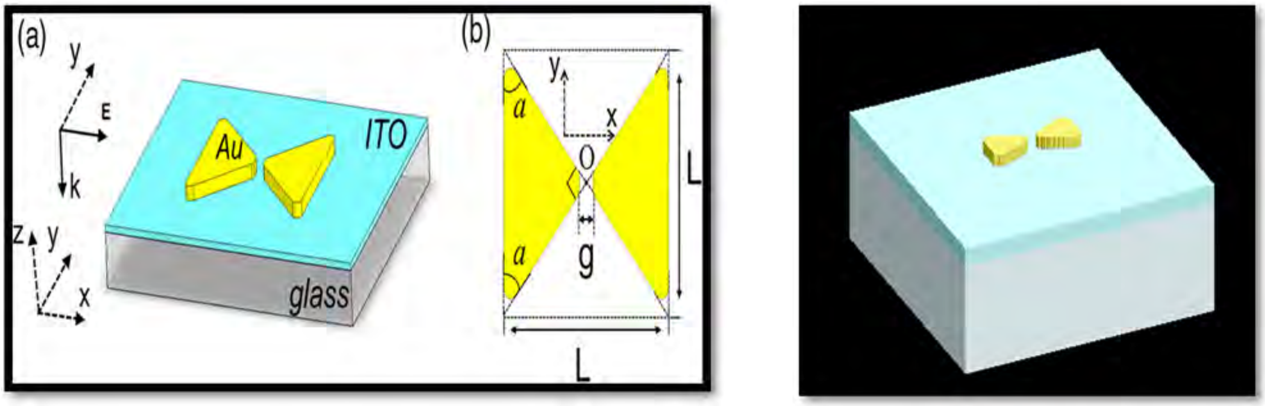

Fig 5.3 Schematic of the structures

Fig 5.3 (a) shows geometry of the structure and (b) Schematic of the structure (right**)**

5.3 FDTD Solver

The 2D/3D FDTD solver region defines many important simulation parameters including simulation volume, boundary conditions, simulation time, and mesh size.

5.3.1 General and Geometry

The dimension of the simulation region was selected to be 3D as our designed structure is three dimensional while the background index was set at 1.33, that of water, which is later, varied. The background index of a solution in the FDTD solver signifies that the entire structure is immersed in that solution. Next the simulation time was set to 500s. This is the maximum duration of the simulation to be performed. The actual simulation may be shorter if the auto shutoff criteria are satisfied before this maximum simulation time is exceeded.

The dimensions of the simulation region is set to 1000nm on the x,y and z spans so that it covers the entire structure to be simulated.

5.3.2 Boundary Conditions

5.3.2.1 Perfectly Matched Layer

By construction, PML absorbing boundary conditions are impedance matched to the simulation region and its materials. This allows them to absorb light waves (both propagating and evanescent) with minimal reflections. An ideal PML boundary produces zero reflections, however, in practice, there will always be small reflections due to the discretization of the underlying PML equations. Furthermore, as a consequence of using finite difference approximations to discretize the PML equations, there is some chance of producing numerical instabilities. The goal of this section is to outline best practices for minimizing reflection errors and getting rid of numerical instabilities without increasing simulation times unnecessarily.

We have used “stretch coordinate PML” and the same settings on all boundaries. This is because, unlike conventional boundary conditions, PML boundaries have a finite thickness. In other words, they occupy a finite volume that surrounds the simulation region. It is within this volume that the absorption of light happens

5.3.2.2 Extending structure through PML

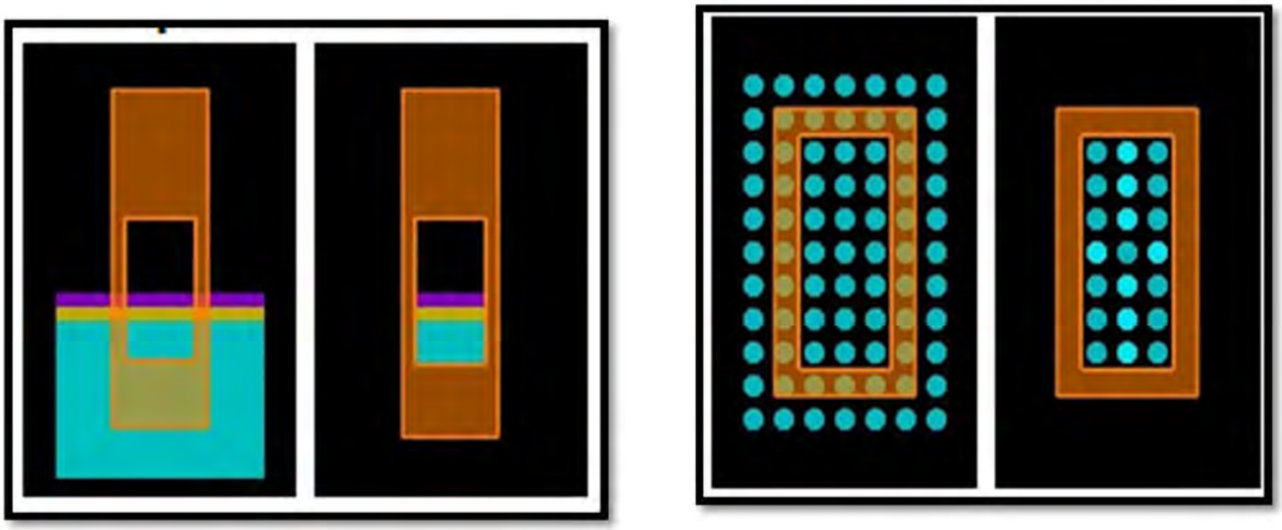

Fia 5.4 Schematic of PML

The figure above shows schematic of PML in single (left) and periodic structure (right).

PML boundary conditions are designed to absorb all incident light. For best performance, physical structures should extend completely through the PML boundary condition region. The default settings in FDTD will automatically extend any structures which lie on the PML boundary through the PML. In some cases, such as for photonic crystals, it is better to disable this feature and draw the structures in the PML manually.

During a simulation, the electromagnetic fields are calculated both within the simulation area (A) and within the boundary condition area (B). Since the fields are still being propagated in (B), it is important that the material properties are also defined here. An interface in this area will act like any other interface and cause reflections. All structures should extend completely through the boundary condition area to minimize these reflections. This is especially important when using many layers of PML. As more layers of PML are added, the boundary condition area will become larger. [32]

Figure (left) shows the setup we used as we used substrates and other layers with PML. The layers extended through the PML in both the X and Y directions. Figure (right) shows the layers terminated at the inside boundary of the PML. This interface may create an undesired reflection. As we have selected the extend structures through PML option, FDTD Solutions will automatically extend the structure in the right figure so that it gives the same results as the left figure. Figure (5.4) shows the correct setup when using periodic structures with PML. The structures should extend through the PML boundary. Figure (right) shows the periodic structure only defined within the simulation volume. This effectively creates an impedance mismatch between the PC region and the boundary condition region. The mismatch reduces the performance of the PML.

5.3.2.3 Periodic

When studying periodic systems, Periodic BC's allow you to calculate the response of the entire system by only simulating one unit cell. Periodic BC's are relatively straightforward to use in the simulation: simply set the simulation span to be one unit cell wide and select Periodic BC's for that boundary. When the simulation runs, the Periodic BC's simply copy the EM fields that occur at one side of the simulation

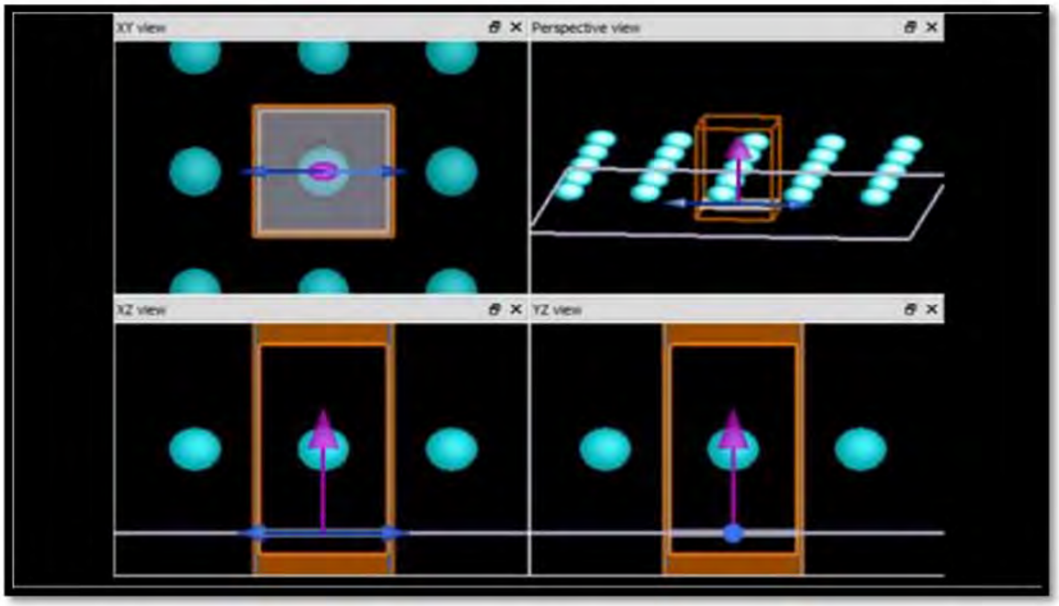

Fig 5.5 Periodic Boundary Condition

and inject them at the other side. The most important detail to remember is that when using periodic BCs, everything in the system must be periodic: both the physical structure and the EM fields. A common source of error is to use periodic conditions in systems where the structure is periodic but EM fields are not. [27]

The following section will deal with the Symmetric Boundary Condition. In our simulation for periodic array, we used Symmetric Boundary Conditions. Fig 5.5 shows a schematic of Periodic Boundary Condition

Rules of symmetry in Symmetric Boundary Conditions:

Symmetric boundary condition can be used whenever the EM fields have a plane of symmetry through the middle of the simulation region. By taking advantage of this symmetry, the simulation volume and tie can be reduced by factors of 2, 4 or 8. This topic describes the difference between symmetric and anti-symmetric boundary conditions, and how to select the appropriate boundary of our simulation. [29]

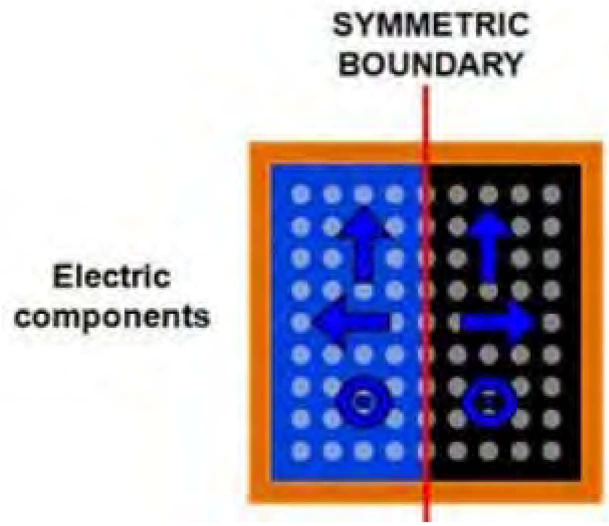

Fig 5.6 Rules of Symmetry

The electric and magnetic fields will obey certain symmetry rules with respect to reflections through the plane of symmetry. The reflection symmetry rules are shown in the figure.

5.4 Mesh Analysis

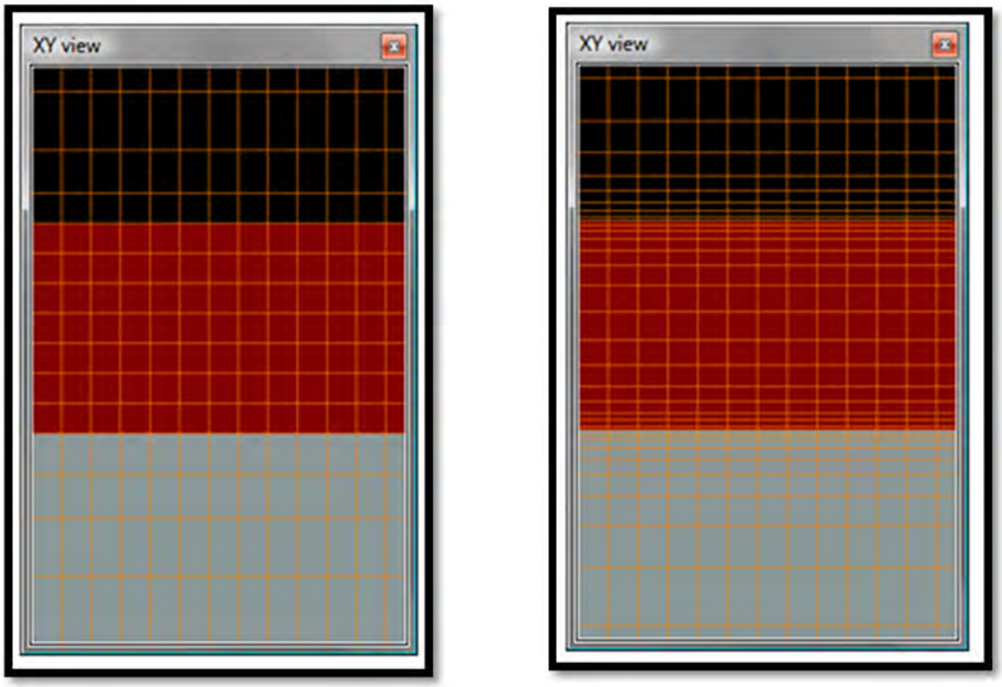

Fig 5.6 Schematics of Mesh

Fig 5.6 shows Schematic of conventional mesh (left) and gridded mesh (right).

For our designed structure, we have used a mesh for the bowtie gap between the two polygons and another rectangular mesh that covers both the polygons completely. For the bigger mesh of the antenna, the override x. y and z meshes were fixed at 2nm in size, while the mesh size of the gap was fixed at 1nm. The mesh sizes were chosen with the simulation time and memory requirements in mind. As a result, we use a combination of combination of graded meshing and conformal meshing. The conformal meshing allows us to obtain more accurate results for a given mesh size. Even if the mesh size is only twice as large, for example 2nm compared to 1nm, the computation time in 3D simulations can be reduced by a factor of 16. [28]

The following table shows the relationship between mesh size and simulation time and memory requirements

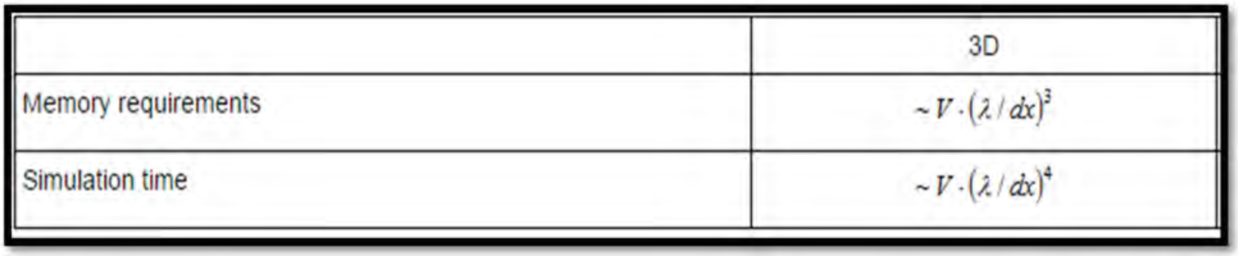

	3D
Memory requirements	$\sim V \cdot (\lambda / dx)^3$
Simulation time	$\sim V \cdot (\lambda / dx)^4$

5.5 Source – TFSF

For the purpose of illuminating our experimental setup, we have used total-field scattered-field (TFSF) source with a wavelength range from 450 nm to 1000 nm. It must be noted that, we have placed the source both parallel (TM) and perpendicular (TE) to the major axis of the structure, in order to investigate the different simulation results.

5.5.1 Transverse Electric and Transverse Magnetic Modes

Transverse electric (*TE*) *modes* is when no electric field is in the direction of propagation. These are sometimes called *H modes* because there is only a magnetic field along the direction of propagation (*H* is the conventional symbol for magnetic field).

Transverse magnetic (*TM*) *modes* are when there is no magnetic field in the direction of propagation. These are sometimes called *E modes* because there is only an electric field along the direction of propagation.

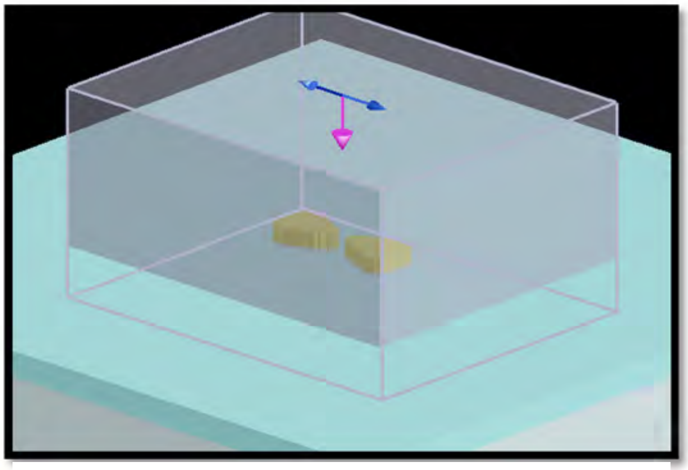

Fig 5.7(a) Structural Model

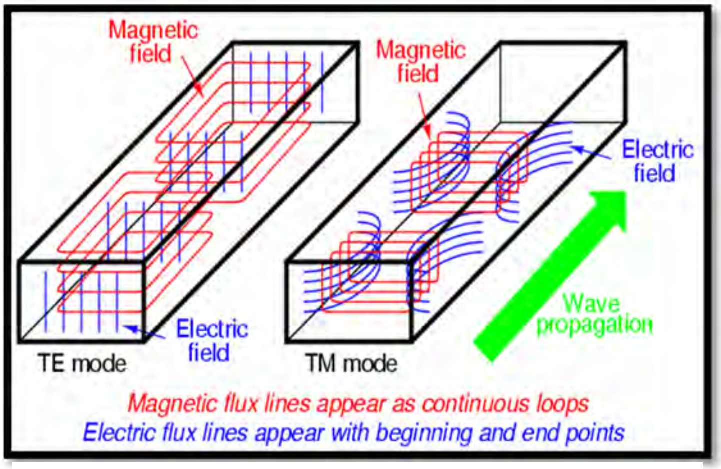

Fig 5.7(b) TE and TM modes

Fig 5.7 9(a) shows the schematic of structural model with source and 5.7 (b) shows TM and TE modes.

The TFSF source allows you to separate the computation region into two distinct regions: Total Field region, which includes the sum of the incident field wave plus the scattered field, and the Scattered Field region which includes only the scattered field, which we separated using monitors discussed in the next section.

5.6 Monitors and Analysis Group

5.6.1 Monitors

In order to obtain results, we have used frequency-domain field monitors and index monitors as first. Frequency domain field monitors require large amounts of memory when recording data over a large spatial domain. Thus we use 2D rather than 3D monitors. Similarly, we try to minimize the number of frequency points recorded.

We then use the index monitor to record the n and k value as a function of frequency or wavelength in the simulation. Index monitors are only available in two or three dimensions; there is no option for linear or point index monitors, thus we use modest memory requirements. To minimize the amount of memory required, we use 2D rather than 3D monitors. Similarly, we minimize the number of frequency points recorded. By default, only one frequency point is recorded.

5.6.2 Analysis Group

The absorption cross section (the rate at which energy is removed from the incident plane wave by absorption) is calculated by an analysis group located inside the TFSF source. The analysis group calculates the net power flow into the particle and hence the absorption cross section using the optical theorem. Similarly, the scattering cross section is calculated by an analysis group located outside the TFSF source. This group measures the net power scattered from the particle. To obtain these plots, we increase the number of *frequency points* from *global monitor settings* to 50 from the Edit tab of x-normal-profile.
The extinction cross-section is the sum of the absorption and scattering cross-sections. [31]

Fig 5.8(a) Cross Section Analysis

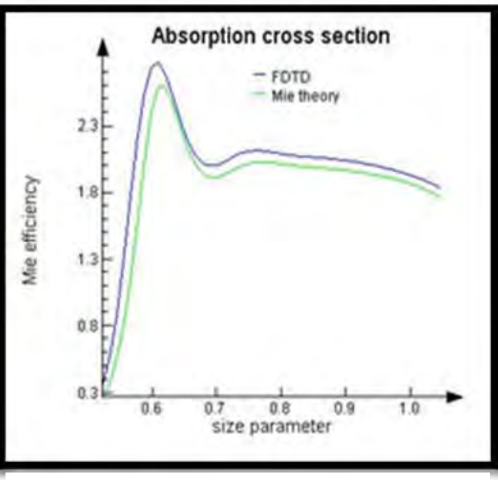

Fig 5.8(b) Absorption Cross Section

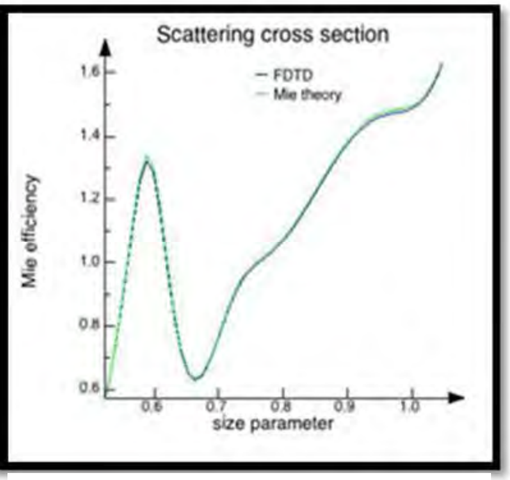

Fig 5.8(c) Scattering Cross Section

Fig 5.8 (a) shows the schematic of Cross Section Analysis (b) Absorptions (c) Scattering cross section.

5.7 Summary

Lumerical develops photonic simulation software – tools which enables product users to understand light, and predict how it behaves within complex circuits, structures and systems.

We have used FDTD Solutions in our thesis paper in order to simulate and analyze the results obtained from isolated bowtie structure and bowtie array. We have accurately designed the surrounding, substrate material, direction of incident light and electric field for our research.

The General settings allow us to choose the material(s) the nanoparticle is to be made of and the dimensions of it. The FDTD option provides us with General, Geometry, Boundary Conditions and a lot more. However, we focus on these three only. In every part, Geometry allows us to vary the values of the boundary. General settings are used to vary the surroundings as well as the angles (or direction). Finally, Boundary Conditions allow us to simulate certain parts of the experimental setup. For instance, if we go for the Symmetric option, the software automatically simulates half of the setup, and arithmetically doubles the value and displays the total result. Mesh Analysis is used for smooth curves.

The smaller the value of Mesh, the smoother the curve will be in expense of simulation time and memory requirements.

Substrate is the bottom layer for any kind of stricture. For our research, we have used Silicon Dioxide (SiO2) as our substrate.

For the source, we have used TFSF (Total Field Scattered Field) light in both parallel and perpendicular to the major axis. Finally for results, we used the results obtained from Cross Section Analysis group, obtaining Extinction curves.

6.0 Simulation and Results

6.1 Introduction

After completing the design of our isolated gold bowtie nanoantenna structure and gold bowtie nanoantenna array, we run the simulation several times, changing various factors each time and observing the results. Our analysis was based on results we obtained from the cross section analysis monitors and the reflectance power monitors.

We have investigated and analyzed the results based on the following variant factors.

- We ran simulations for two polarizations of the incident light: parallel to the major axis(TM) wave and perpendicular to the major axis, keeping the geometry and medium constant.
- We varied the gap size between the two polygons from 5 nm to 100nm, for polarizations parallel and perpendicular to major axis, keeping the geometry of our structure constant.
- We varied the corner radius, r, of our nanostructure from 0 to 90 nm, for incident light parallel to major axis(TM).
- For the bowtie nanoantenna array structure, we varied the pitch distances (center to center distance) in both x and y directions, hence varying Dx and Dy distances to change the pitch distance between the bowtie antennas.
- For a certain pitch distance of the nanoantenna array structure, we varied the refractive index of the surrounding medium for parallel polarization, keeping all other factors constant.

6.2 Results Analysis

6.2.1 Varying Gap Size

Keeping all other geometric parameters at our baseline values, we carried out simulations for various gaps of the isolated bowtie structure, varying from 5nm to 100 nm. We initially changed the gap size for polarization parallel (TM) to the bowtie structure and calculated the extinction spectra, analyzing the plasmon peak shift and the width.

We then carried out simulations for the same gap sizes, but with incident light perpendicular to major axis (TE), further analyzing the different plasmon peaks.

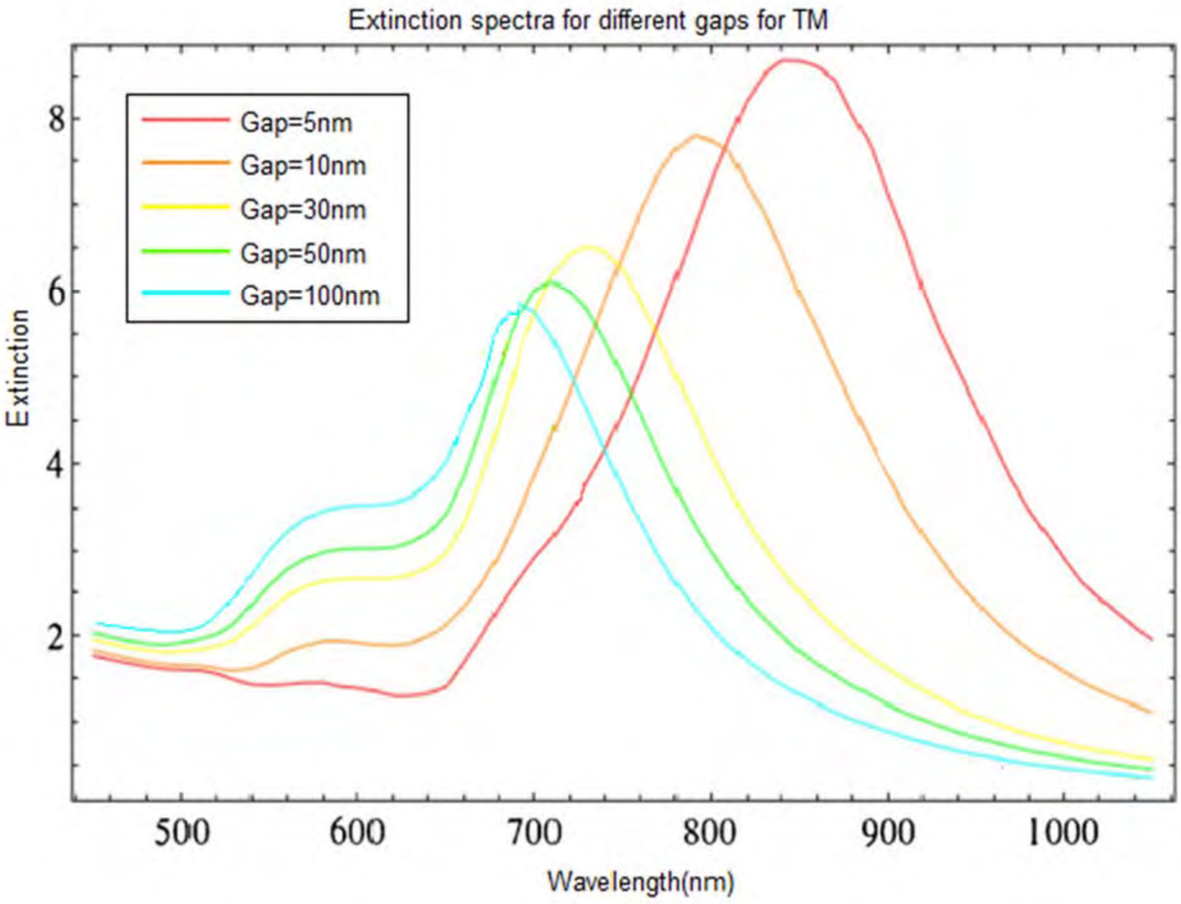

Fig 6.1 Extinction spectra for different gaps for TM

We carried out simulations varying the bowtie gap from 5nm to 100 nm for both polarizations. As the electric field profiles show, when the source is incident such that the electric field is parallel to the major axis of the bowtie structure, it results in a high confinement of electric field within the gap region of the nanoantenna. However, if the polarization is perpendicular, the confinement of the electric field, also said to enhancement areas occurs around the other tips of the bowtie which is far from the gap region. [41]

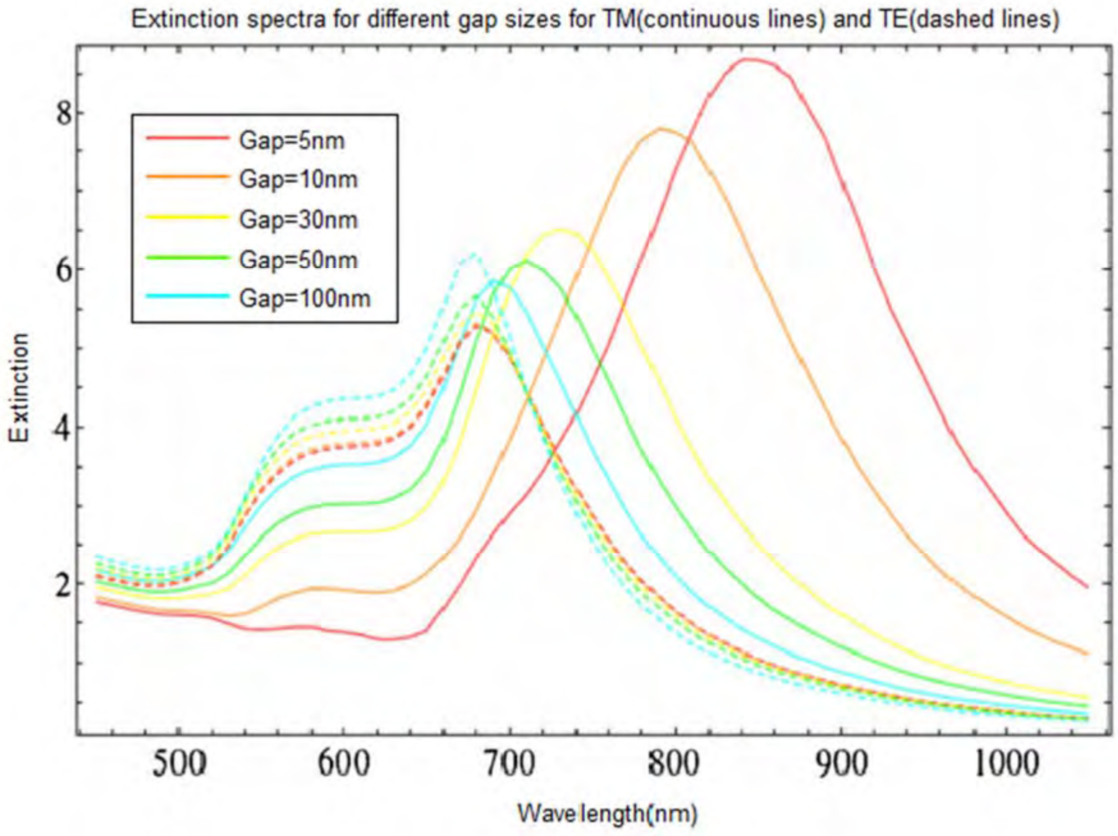

Fig 6.1 Extinction spectra for varying gaps for TM

Fig 6.2 shows Extinction spectra for different gap sizes for TM (continuous lines) and TE (dashed lines)

From the figure (6.2) it can be observed that the increasing redshift occurs with smaller gap size for TM wave, polarization parallel to the major axis. While the redshift for TE wave, polarization perpendicular to the major axis is almost negligible. The latter is short wavelength Plasmon resonance and the former is longer wavelength Plasmon resonance. The extinction efficiencies we obtained are thus consistent with other results obtained for different nanostructures. [44]

As observed from the graphs we obtained the extinction curves tend to converge as the gap increases. Furthermore, the redshift of TE mode is insignificant. Both of the phenomenon can be explained by the direct dipolar coupling being weak between two particles. And so when the bowtie gap distance is sufficiently small, the electric field enhancement increases. [45]

6.2.2 Different corner radii for the polygons

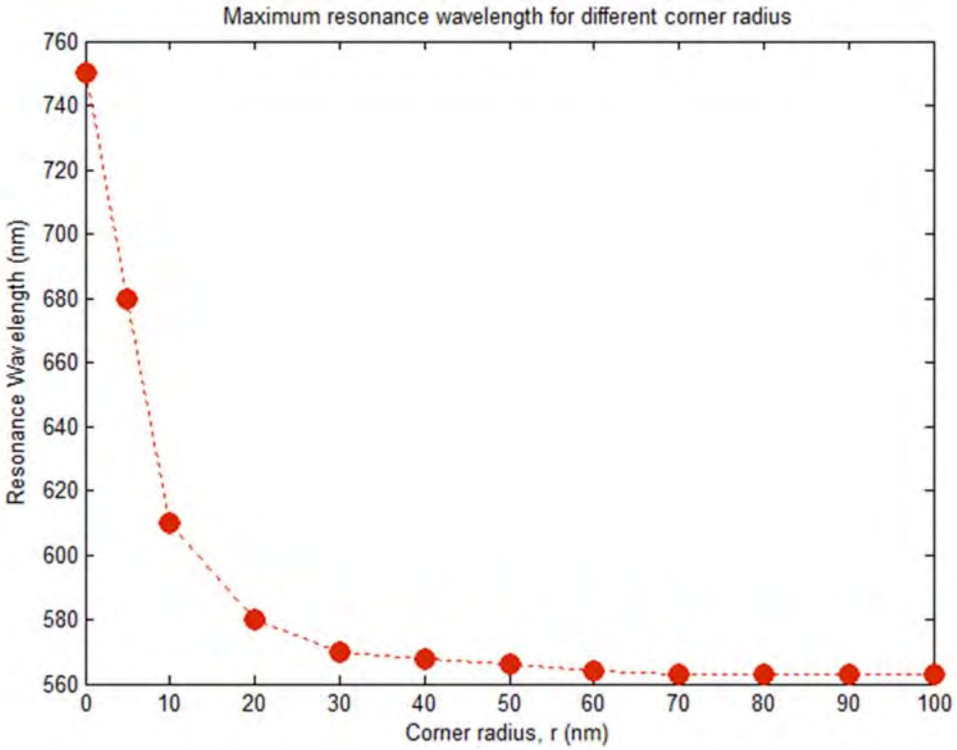

Fig 6.3 Resonance peak vs. corner radius

For a fixed gap size, 30 nm for our case, we vary the radius of our bowtie nanostructure from 0 nm (sharp edges) too 100nm. For this we have used the image extraction option in FDTD solver of Lumerical. For each corner radius we obtain a maximum resonance wavelength, show in Fig (6.3). It is observed that there is a slight blue shift with increasing corner radius. This is explained by the Coulombic restoring force. Unlike the bowtie with 0 corner radius (sharp edge), the ones having a rounded edge, have greater charge separation in them, resulting in a higher oscillation frequency and hence the resonance peak is shifted to shorter wavelength. The charges on metal structures tend to concentrate at sharp corners. [40]

6.2.3 Different pitch distance

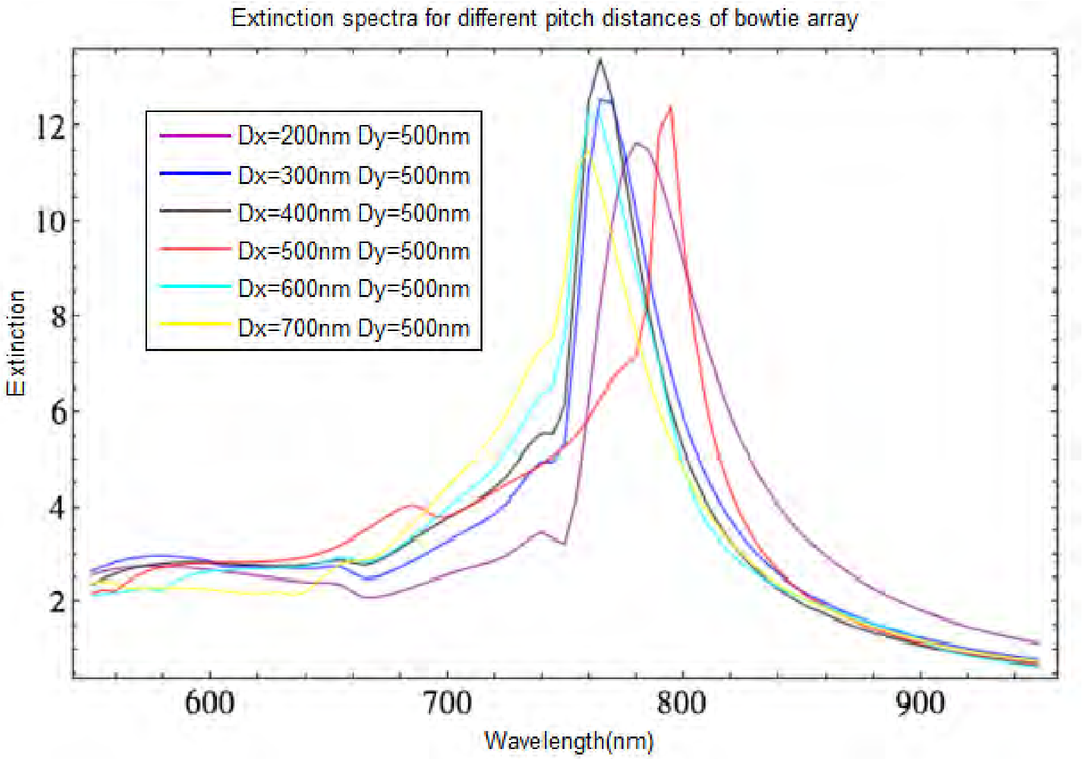

Fig 6.4 Extinction spectra for array

For a certain gap size (30nm) and geometry of the bowtie, we created our array of bowtie nanostructure with varying center to center distance. The pitch distances were varied in horizontal direction (Dx), keeping the vertical distance (Dy) constant at 500nm. Figure (6.4) shows our simulation results.

Fig 6.4 shows the extinction spectra for varying pitch distances of bowtie array structure. Here, we varied the pitch distances such that we get the narrowest plasmon peak around 790nm for polarization parallel to major axis and hence obtain the best sensitivity at this wavelength. As we can see from our simulation result, when Dy is fixed and Dx is decreased, a noticeble red shift and broadening occurs. This agrees with our previous finding of the single bowtie with varying gap size.

If the wavelength of the scattered light is close to both the pitch distances of the array and the LSPR wavelength, then, a dramatic modification of the extinction cross section will arise due to a collective coupling of every localized plasmon. When excited by an EM wave at frequency ω, a dipole radiates a scattered wave proportionally to its dipole moment and so the net field at every dipole is therefore the sum of the incident field plus the radiation of all the others dipoles. Hence, creating narrowing resonance. [42]

6.2.4 Varying Refractive Index of the surrounding medium

We varied the refractive index of the surrounding medium from 1.33 to 1.55. The following solutions were used in our simulations.

- Water (n=1.33)
- Ethanol (n=1.36)
- Glucose solution in water (n=1.40)
- PMMA solution (n=1.47)
- Benzene (n=1.55)

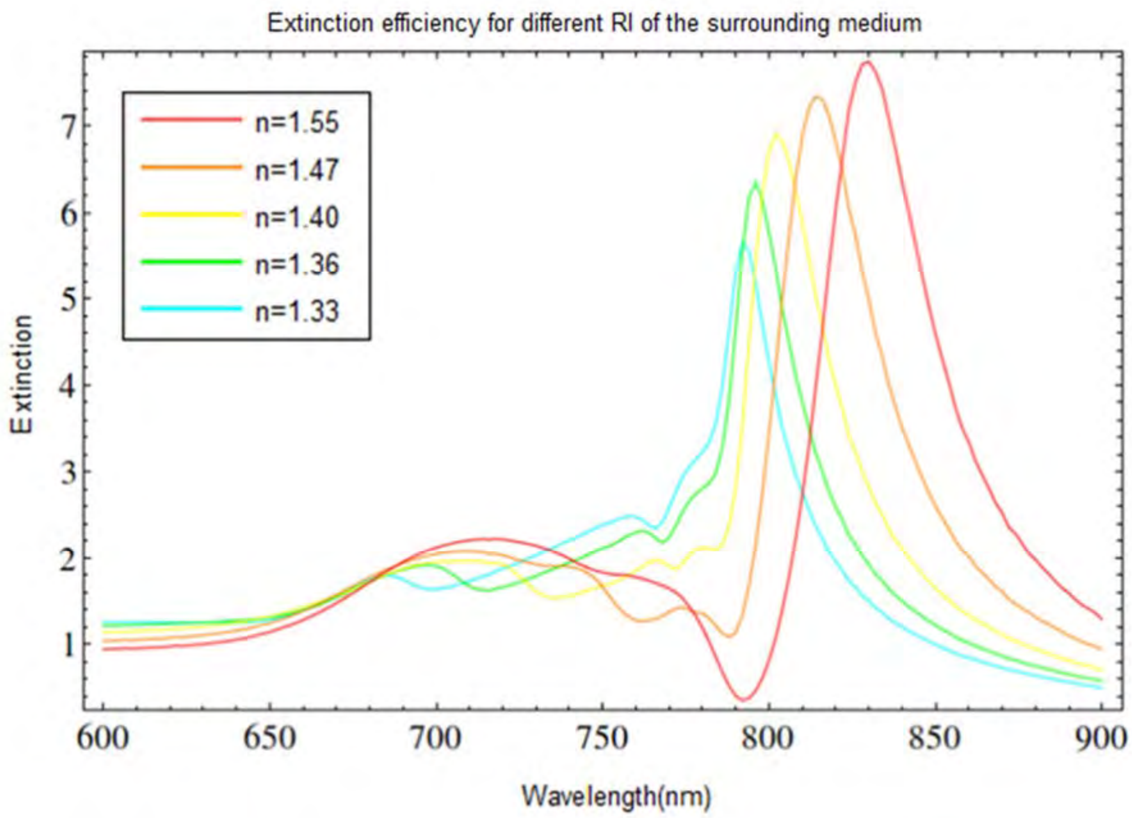

Fig 6.5 Extinction for different refractive index.

2.4.1 Bulk refractive index sensing

We study the variation in the obtained extinction peaks with respect to different refractive index of the surrounding medium. Fig 6.5 shows the extinction spectra for different refractive index. The results for bowtie array were obtained and then compared to that of the isolated structure. Below a table of results, followed by a graph including the different refractive indexes and the wavelength the primary peak was found at for those refractive indexes are included. As well as the SPR shifts found for the refractive indices are mentioned.

Table of Results:

Refractive index, n	**Peak Wavelength (nm) of bowtie array, λ1**	**Peak Wavelength (nm) of single bowtie, λ2**	**SPR Shift (nm) (dλ1) of λ1**	**SPR Shift (nm) (dλ2) of λ2**
1.33	786.01nm	730.04nm	00.00nm	00.00nm
1.36	796.23nm	740.07nm	10.22nm	10.03nm
1.40	806.10nm	750.11nm	20.09nm	20.07nm
1.47	819.35nm	763.23nm	33.34nm	33.19nm
1.55	830.04nm	778.00nm	44.03nm	48.01nm

Graphical Representation:

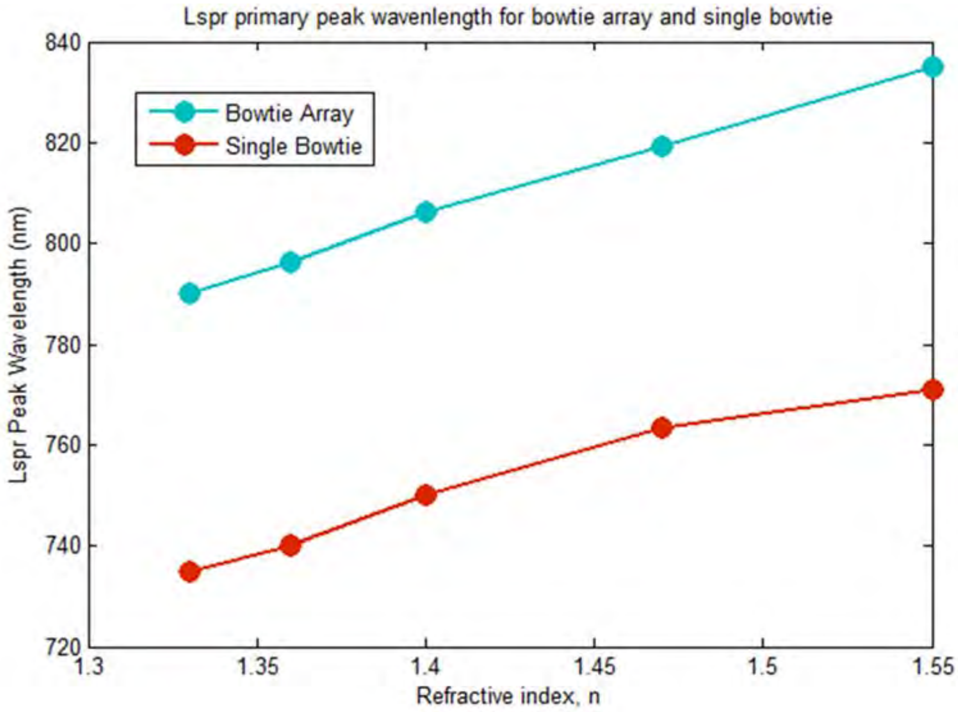

Fig 6.6 LSPR peak vs. RI for both structures

Fig 6.6 shows the Lspr primary peak against refractive index.

The sensitivity of the system is defined by the change in Lspr peak wavelength with respect to refractive index.

$$S = \frac{\partial \lambda_{LPSR}[nm]}{\partial n[RIU]}$$

Calculation:

1. Sensitivity for bowtie array = (830.04-786.01) ÷(1.55-1.33)
   = 200.14

2. Sensitivity for single bowtie= (778.00-730.04) ÷(1.55-1.33)
   = 218.22

From the figure above, where Lspr wavelength is plotted against refractive index of the surrounding medium for both bowtie array and single bowtie, we observe that the slope for single bowtie is slightly greater than that of the array. As the calculations show, the sensitivity of single bowtie is thus, higher than that of array, considering the Lspr red shift.

6.2.5 Bimolecular Surface Sensing

In order to analyze the surface sensitivity of bio detectors, we carried out a series of simulations by adding additional bound layer of bio receptors and analytes having different refractive index. As most bioassays tend to capture analyte within the first15 to 20 nm from the surface of the nanoantenna, we used a bio receptor and analyte layer of thickness 5nm. [35] The bio receptor is the first layer; hence we used an acceptable constant RI of 1.39. However, the second analyte layer was varied in order to obtain our results. The simulation for surface sensing was done for both parallel and perpendicular polarizations and the results, later compared.

For parallel polarization (TM):

Table of Results

Medium	**Refractive Index, n**	**Peak Wavelength (λ)**	**SPR Shift (dλ)**
H2O	1.33	793.22nm	**0.000**
Fb	1.39	795.08nm	**1.860**
HAS	1.44	797.55nm	**4.330**
LyS	1.50	799.03nm	**5.810**

Graphical Representation:

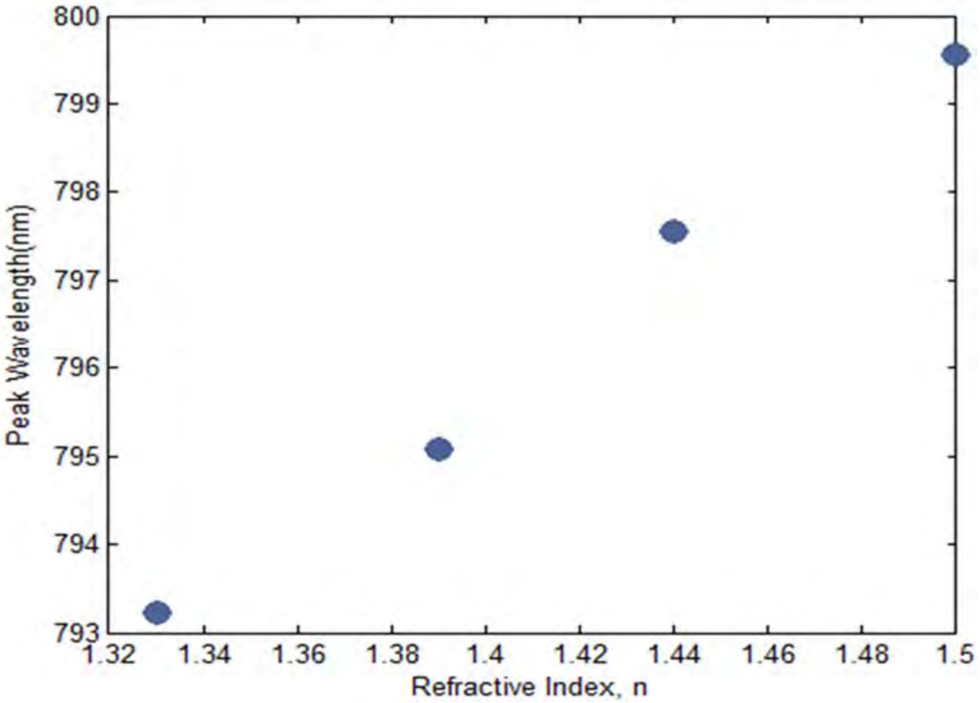

Fig 6.7 LSPR peak vs. RI for TM

Fig 6.7 shows the Peak Wavelength against Refractive index for parallel polarization.

For perpendicular polarization (TE):

Table of Results

Medium	Refractive index, n	Wavelength (λ)	SPR Shift (dλ)
H2O	1.33	760.42nm	**0.000**
Fb	1.39	761.01nm	**0.590**
HAS	1.44	762.43nm	**2.010**
Lys	1.50	764.03nm	**3.610**

Graphical Representation

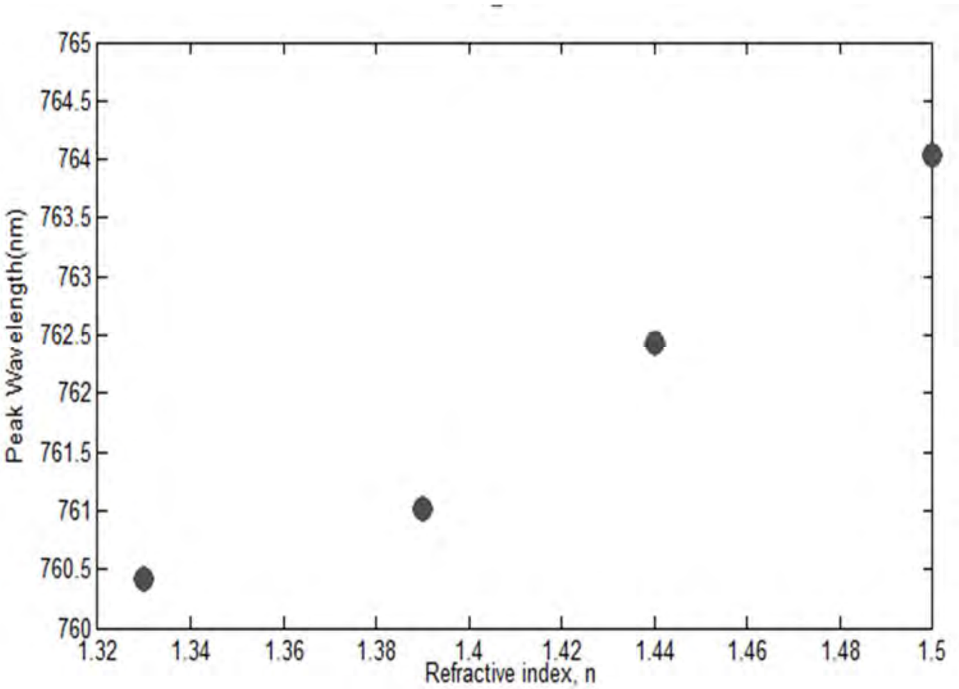

Fig 6.8 LSPR peak vs. RI for TE

Fig 6.8 show the Peak Wavelength against Refractive Index for perpendicular polarization**.**

For both cases, we observed that the biomolecular coating leads to the redshift of the resonance wavelength, as reflected in Fig. 6.8 and 6.9. This can be explained by the increase of the effective optical path caused by the larger refractive indices of the coating. [46]

7. CONCLUSION

In our paper, we study the unique characteristics of Local Surface Plasmon Resonance (LSPR). Among the various applications of LSPR in the fields of photo catalysis, medicine and photovoltaics, we have focused on biosensing. From our work, we have observed that LSPR spectroscopy of metallic nanoparticles is a powerful technique for chemical and biological sensing experiments.

Our paper was based on a gold bowtie structure. The nanoparticles which were modeled as equilateral triangles, deposited on ITO / glass with a thickness of 4000 nm and a titanium adhesion layer of 3 nm of thickness was added under the gold nanoparticles. The entire structure was immersed in different solutions of varying refractive index, starting with water (n=1.33). The TFSF source with a wavelength range from 450 nm to 1000 nm was placed both parallel (TM) and perpendicular (TE) to the major axis of the structure.

For results, we ran the simulation several times, changing various factors each time and observing the results. Our analysis was based on results we obtained from the cross section analysis monitors.

In conclusion, optical antennas are the prevailing tool for the manipulation of light on a nanometer scale and they are also capable of delivering optimum control over transduction in the far-field region. Present optical antenna research is being motivated in particular by developments in nanofabrication technology and RF antenna analogies. Though various antenna conformations are currently being appreciated in the optical regime, it is going to be fascinating to observe how different antenna parameters, such as the impedance matching, are going to be redefined for different types of optical sources, like atoms and molecules. Optical antennas unite the quantum methods and photon sources by including fascinating new physics, for instance the breach of selection procedures and unconventional ways for robust pairing. The ideas of focused radiation and focused reception can be pragmatic to the photon emitters. Once the techniques of nanofabrication have been become mastered, a variety of applications will appear, including controlled single-photon sources for quantum information, light harvesting, energy conversion, efficient biosensors, data storage, nanoscale optical circuitry and optical imaging beyond 10 nm resolution. Once we have designed an optical antenna for biomedical applications, we must take time for enough study about the possible side effects. Therefore, a proper understanding about the effects of the specific antenna before practical implementation is a prerequisite

This review has emphasized the principle and applications of optical biosensors. An appreciation of optical antenna basics offers chances of tuning and controlling the optical performance. Optical antennas have a robust reliance on the shape, size and composition of the nanoparticles which deliver an enhancement of biosensors' sensitivity. A wide range of investigations on optical antenna are now dedicated to making substrates, which afford solid improvements of the EM field and deliver information about attaining control of optical properties by controlling the physical factors of nanoparticles. In spite of the different challenges for practical implementation of optical biosensors, the technical works show that importance in optical biosensor improvement continues to increase at a tremendous pace.

References

1. Plasmon(2017) Retrieved from https://en.wikipedia.org/wiki/Plasmon
2. *Plasmonics* Retrieved from: https://www.physik.huberlin.de/de.nano/lehre/Gastvorlesung%20Wien/plasmonics
3. Stockman, M. I., (2011). Nanoplasmonics: the physics behind the applications. *Physics Today*, 39-44. Retrieved from: http://physics.gsu.edu/stockman/data/Stockman_Phys_Today_2011_Physics_behind_Applications.pdf
4. Nanoplasmonics: Physics and Applications. Retrieved from https://www.nist.gov/news-events/events/2014/02/nanoplasmonics-physics-and-applications
5. Nanomaterial characterization techniques. Retrieved from http://www.npl.co.uk/science-technology/surface-and-nanoanalysis/services/nanomaterials-characterisation-techniques-for-powders-and-liquid-dispersions
6. Ali, M. E.; Hashim, U.; Mustafa, S.; Che Man, Y. B.; Islam, Kh. *N. Journal of Nanomaterial 2012*, 2012, Article ID 103607
7. Maier, S. A. (2007) Localized Surface Plasmons. *Plasmonics: Fundamentals and applications*, p. 65-72. Retrieved from: https://www.londonnano.com/sites/default/files/uploads/research/highlights/Nanoplasmonics/pdf
8. Surface Plasmon Resonance. Retrieved from: https://en.wikipedia.org/wiki/Surface_plasmon_resonance
9. Localized Surface Plasmon Resonance Theory. *Localized Surface Plasmon Resonance vs. Surface Plasmon Resonance*. Retrieved from: https://nicoyalife.com/technology/surfaceplasmon-resonance/localized-surface-plasmon-resonance-theory/
10. Stefan Maier (2007). *Plasmonics: Fundamentals and Applications*. Springer
11. Localized Surface Plasmon Resonance. Retrieved from https://en.wikipedia.org/wiki/Localized_surface_plasmon

12. The Lycurgus Cup-A Roman Nanotechnology. Retrieved from https://www.researchgate.net/publication/216212135_The_Lycurgus_Cup-A_Roman_Nanotechnology
13. Pierre-Arnaud Raviart and Eric Sonnendrücker, “Approximate models for the Maxwell equations,” J. Comput. Appl. Math. 63, 69–81 1994.
14. Faraday’s law, Ampère’s law and the quasistatic approximation. Retrieved from http://www.physicspages.com/2013/09/27/faradays-law-amperes-law-and-the-quasistatic-approximation/
15. Localized Surface Plasmon Resonance Theory. *Localized Surface Plasmon Resonance vs. Surface Plasmon Resonance*. Retrieved from: https://nicoyalife.com/technology/surfaceplasmonresonance/localized-surface-plasmon-resonance-theory
16. Raether, H. (1988). Surface Plasmons on Smooth and Rough Surfaces and on Gratings. *Springer Tractsin Modern Physics*, Vol. 111, Springer Berlin
17. Mayer, Kathryn M.; Hafner, Jason H. (2011). "Localized Surface Plasmon Resonance Sensors". *Chemical Reviews*. Plasmonics (111)
18. Free electron model (2016). Retrieved from: https://en.wikipedia.org/wiki/Free_electron_model
19. Edward M. Purcell (1965). *Electricity and Magnetism*. McGraw-Hill. pp. 117–122.
20. Drude Model. Retrived from https://en.wikipedia.org/wiki/Drude_model
21. Gold Nanoparticle Properties Retrieved from http://www.cytodiagnostics.com/store/pc/Gold-Nanoparticle-Properties-d2.htm
22. A. Haes and R. Van Duyne, "A unified view of propagating and localized surface plasmon resonance biosensors
23. Karl S. Kunz and Raymond J. Luebbers (1993). *The Finite Difference Time Domain Method for Electromagnetics*
24. Finite-difference time-domain. Retrieved from https://en.wikipedia.org/wiki/Finite-difference_time-domain_method
25. FDTD method. Retrived from https://www.remcom.com/xf-fdtd-method/
26. Lumerical Solutions, Inc. Retrieved from: https://www.google.com/search?q=lumerical+solutions+logo&client=firefoxbab&sourc

e=lnms&tbm=isch&sa=X&ved=0ahUKEwjmxIj54-rQAhWFORoKHfhRBw4Q_AUICCgB&biw=1366&bih=657#imgrc=3iyJWdEBdavy3M%3A

27. Periodic boundary conditions. Retrieved from: https://kb.lumerical.com/en/index.html?ref_sim_obj_symmetric_anti-symmetric.html
28. Mesh refinement. Retrieved from: https://kb.lumerical.com/en/index.html?ref_sim_obj_symmetric_anti-symmetric.htm
29. Symmetric and anti-symmetric BCs. Retrieved from: https://kb.lumerical.com/en/index.html?ref_sim_obj_symmetric_anti-symmetric.html
30. About Lumerical Retrived from https://docs.kogence.com/docs/Lumerical_Mode_Solutions
31. Analysis Group. Retrived fromhttps://kb.lumerical.com/en/ref_sim_obj_analysis_groups.html
32. Extending Structures through PML/ Retrived from https://kb.lumerical.com/en/ref_sim_obj_extending_structures_through_pml.htmls
33. Jain, P.K.; Lee, K.S.; El-Sayed, I.H.; El-Sayed, M.A. Calculated Absoprtion and Scattering Properties of Gold Nanoparticles of Different Size, Shape and Composition: Applications in Biological Imaging and Biomedicine. J. Phys. Chem. B 2006
34. Sagle, L.B.; Ruvuna, L.K.; Ruemmele, J.A.; van Duyne, R.P. Advances in localized surface plasmon resonance spectroscopy biosensing. Nanomedicine 2011, 6, 1447–1462
35. Mayer, K.M.; Hafner, J.H. Localized Surface Plasmon Resonance Sensors. Chem. Rev. 2011, 111, 3828–3857.
36. Kelly, K. L., Coronado, E., Zhao, L. L. & Schatz, G. C. (2003). The optical properties of nanoparticles: The influence of size, shape, and dielectric environment. *J. Phys. Chem*. B 107, 668-677
37. Hohenester, U. & Krenn, J., (2005). Surface plasmon resonances of single and coupled metallic nanoparticles: A boundary integral method approach. *Phys. Rev. B* 72, 195429.
38. Chen, Wen-Yu; Lin, Chun-Hung. (2010). Estimation of Electric Fields at Bow-tie Antenna
    Gaps.

39. Shlager, K. L. et al., "Optimization of bow-tie antennas for pulse radiation," *IEEE Trans. Antennas and Propagate.* Vol. 42, No. 7, 975–982, Jul. 1994.
40. Chao, Bo-Ki; Lin, Shih-Che,Li, Jia-Han.(2015). Effects of corner radius on periodic nanoantenna for surface-enhanced Raman spectroscopy.
41. A. Sundaramurthy *et al.*, "Field enhancement and gap dependent resonance in a system of two opposing tip-totip Au Nano triangles," *Physical Review B*, vol. 72, pp.165409, 2005.
42. Sharma, H; Sharac,N; Ragan,R; Veysi,M. (2016). Tunable optical response of bowtie nanoantenna arrays on thermoplastic substrates. Nanotechnology, vol 27. Number 10.
43. Chen, Hao; Bhuiya, Abdul; Wasserman, Daniel.(2014). Design, Fabrication, and Characterization of Near-IR Gold Bowtie Nanoantenna Arrays. *J. Phys. Chem. C*, 2014, *118* (35), pp 20553–20558
44. Hatab, Nahla; Li, Jia-Han; Eres, Gyula & Gaddis,Abigail (2010) Free-Standing Optical Gold Bowtie Nanoantenna with Variable Gap Size for Enhanced Raman Spectroscopy.*Nano Lett.*, 2010, *10* (12), pp 4952–4955.
45. Kelly, K. L., Coronado, E., Zhao, L. L. & Schatz, G. C. (2003). The optical properties of nanoparticles: The influence of size, shape, and dielectric environment. *J. Phys. Chem*. B 107, 668-677
46. Lin T-R, Chang S-W, Chuang SL, Zhaoyu Z, Schuck PJ (2010) Coating effect on optical resonance of plasmonic Nano bowtie antenna. Appl Phys Lett 97:063106.
47. Paolo Biagioni, Jesting Huang and Bert Hecht, Nanoantennas for visible and infrared radiation, URL https://arxiv.org/pdf/1103.1568.pdf
48. Samir F. Mahmoud ,Nanoantennas; Theory and Applications, URL http://msa.eun.eg/nrsc2015/uploads/kn2.pdf
49. Lukas Novotny and Niek van Hulst, Antennas for light, http://www.optics.rochester.edu/workgroups/novotny/papers/novotny11a.pdf
50. G.V. Naik, Alternative Plasmonic Materials: Beyond Gold and Silver,http://docs.lib.purdue.edu/cgi/viewcontent.cgi?article=2423&context=nanopub

51. Jeffrey N. Anker, W. Paige Hall, Olga Lyandres, Nilam C. Shah, Jing Zhao & Richard P. Van Duyne, Biosensing with plasmonic nanosensors, http://www.nature.com/nmat/journal/v7/n6/full/nmat2162.html?foxtrotcallback=true
52. Manoj B. Gawande, Cu and Cu-Based Nanoparticles: Synthesis and Applications in Catalysis, http://pubs.acs.org/doi/pdfplus/10.1021/acs.chemrev.5b00482
53. Conformal Atomic Layer Deposition of Alumina on Millimeter Tall, Vertically-Aligned Carbon Nanotube Arrays, Kelly L.Stano, http://pubs.acs.org/doi/abs/10.1021/am505107s
54. Zhang X, Rapid detection of an anthrax biomarker by surface-enhanced Raman spectroscopy, https://www.ncbi.nlm.nih.gov/pubmed/15783231
55. Biosensors – Types, How Does it Works and Applications, https://www.edgefx.in/biosensors-types-its-working-and-applications/
56. Ercole C., Del Gallo M., Mosiello L., Baccella S., Lepidi A. *Escherichia coli* detection in vegetable food by a potentiometric biosensor. Sens Actuators B: Chem. 2003; 91:163–168.
57. Scognamiglio V., Pezzotti G., Pezzotti I. Biosensors for effective environmental and agrifood protection and commercialization: from research to market. Mikrochim Acta. 2010; 170:215–225.
58. Parikha Merhotra Biosensors and their applications – A review, https://www.ncbi.nlm.nih.gov/pmc/articles/PMC4862100/
59. Taerin Chung, Seung-Yeol Le, Eui Young Song, Honggu Chun and Byoungho Lee, (2011). Plasmonic Nanostructures for Nano-Scale Bio-Sensing
60. Biomolecule (2016). Retrieved from: https://en.wikipedia.org/wiki/Biomolecule
61. Lysozyme (2016). Retrieved from: https://en.wikipedia.org/wiki/Lysozyme
62. Human Serum Albumin (2016). Retrieved from: https://en.wikipedia.org/wiki/Human_serum_albumin
63. Fibrinogen Retrieved from: https://en.wikipedia.org/wiki/Fibrinogen
64. Mckeen, Thomas; Grooves, Merton. (1964). Refractive Indices of Amino Acids, Proteins, and Related Substances, *Advances in Chemistry*, Vol. 44.
65. Sagle, L.B.; Ruvuna, L.K.; Ruemmele, J.A.; van Duyne, R.P. Advances in localized surface plasmon resonance spectroscopy biosensing. Nanomedicine 2011, 6, 1447–1462

66. Endo, T.; Kerman, K.; Nagatani, N.; Takamura, Y.; Tamiya, E. Label-free detection of peptide nucleicacid-DNA hybridization using localized surface plasmon resonance based optical biosensor. Anal. Chem. 2005, 77, 6976–6984.
67. Mathers, C.D.; Loncar, D. Projections of global mortality and burden of disease from 2002 to 2030. PLoS Med. 2006, 3, e442, doi:10.1371/journal.pmed.0030442.
68. Hiep, H.M.; Nakayama, T.; Saito, M.; Yamamura, S.; Takamura, Y.; Tamiya, E. A microfluidic chip based on localized surface plasmon resonance for real-time monitoring of antigen-antibody reactions. Jpn. J. Appl. Phys. 2008, 47, 1337–1341.
69. Park, T.J.; Lee, S.J.; Kim, D.K.; Heo, N.S.; Park, J.Y.; Lee, S.Y. Development of label-free optical diagnosis for sensitive detection of influenza virus with genetically engineered fusion protein. Talanta 2012, 89, 246–252.
70. Yousef, A.E. Detection of bacterial pathogens in different matrices: current practices and challenges. In Principles of Bacterial Detection: Biosensors, Recognition Receptors and Microsystems; Zourob, M., Elwary, S., Turner, A.P.F., Eds.; Springer: New York, NY, USA, 2008; pp. 31–48.
71. Junxue, F.; Bosson, P.; Yiping, Z. Limitation of a localized surface plasmon resonance sensor for Salmonella detection. Sens. Actuator. B Chem. 2009, 141, 276–283.
72. Huang, H.; Liu, F.; Huang, S.; Yuan, S.; Liao, B.; Yi, S.; Zeng, Y.; Chu, P.K. Sensitive and simultaneous detection of different disease markers using multiplexed gold nanorods. Anal. Chim. Acta 2012, 755, 108–114.
73. Lee, J.H.; Kim, B.C.; Oh, B.K.; Choi, J.W. Highly sensitive localized surface plasmon resonance immunosensor for label-free detection of HIV-1. Nanomedicine 2013, 9, 1018–1026.
74. Tarparelli, R.; Lovine, R.; Vegni, L. Optical Sensor Based on LSPR Phenomenon to Reveal Cholesterol Concentrations for Biomedical Applications. Presented at the Progress in Electromagnetics Research Symposium Proceedings, Stockholm, Sweden, 12–15 August 2013; pp. 797–800.
75. Goodall, B.L.; Robinson, A.M.; Brosseau, C.L. Electrochemical-surface enhanced Raman spectroscopy (E-SERS) of uric acid: A potential rapid diagnostic method for early preeclampsia detection. Phys. Chem. Chem. Phys. 2013, 15, 1382–1388.

76. Wang, H.-W., Pasternak, J. F., Kuo, H., Ristic, H., Lambert, M. P., Chromy, B., Viola, K. L., Klein, W. L., Stine, W. B., Krafft, G. A., et al. (2002) Soluble oligomers of b-amyloid (1-42) inhibit long-term potentiation but not long-term depression in rat dentate gyrus. Brain Res. 924, 133–140. Walsh,
77. M., Selkoe, D. J. (2004) Oligomers in the brain: The emerging role of soluble protein aggregates in neurodegeneration. Protein Peptide Lett. 11, 213–228.
78. Lambert, M. P., Viola, K. L., Chromy, B. A., Chang, L., Morgan, T. E., Yu, J., Venton, D. L., Krafft, G. A., Finch, C. E., Klein, W. L. (2001) Vaccination with soluble A oligomers generates toxicity-neutralizing antibodies. J. Neurochem. 79, 595–60
79. Ohta, T.; Ito, M.; Kotani, T.; Hattori, T. Emission enhancement of laser-induced breakdown spectroscopy by localized surface plasmon resonance for analyzing plant nutrients. Appl. Spectrosc. 2009, 63, 555–558.
80. 55. Shimomura, M.; Nomura, Y.; Zhang, W.; Sakino, M, Lee, K.H.; Ikebukuro, K.; Karube, I. Simple and rapid detection method using surface plasmon resonance for dioxins, polychlorinated biphenylx and atrazine. Anal. Chim. Acta 2001, 434, 223–230.
81. 56. Bantz, K.C.; Haynes, C.L. Surface-enhanced Raman scattering detection and discrimination of polychlorinated biphenyls. Vib. Spectrosc. 2009, 50, 29–35.
82. Lin, T.J.; Huang, K.T.; Liu, C.Y. Determination of organophosphorous pesticides by a novel biosensor based on localized surface plasmon resonance. Biosens. Bioelectron. 2006, 22, 513–518.
83. Hammond, J. L., Bhalla, N., Rafiee, S. D. and Estrela, P., Localized Surface Plasmon Resonance as a Biosensing Platform for Developing Countries. URL http://dx.doi.org/10.3390/bios4020172